NASA CONTRACTOR REPORT 177465

Study of Solid State Photomultiplier

K. M. Hays
R. A. LaViolette
Rockwell International Corporation
Science Center
Anaheim, California

Prepared for
Ames Research Center
under Contract NAS2-12400

National Aeronautics and
Space Administration

Ames Research Center
Moffett Field, California 94035

TABLE OF CONTENTS

1.0 SUMMARY

Available SSPM detectors were tested under low-background, low temperature conditions to determine the conditions producing optimal sensitivity in a space-based astronomy system such as a liquid-helium-cooled telescope in orbit. Detector temperatures varied between 6 and 9 K, with background flux ranging from 10^{13} to $<10^{6}$ photons/cm^2-s. Measured parameters included quantum efficiency, noise, dark current and spectral response.

Experimental data were reduced, analyzed and combined with existing data to build the SSPM data base included herein. The results were compared to analytical models of SSPM performance where appropriate models existed.

Analytical models presented herein were developed to be as consistent with the data base as practicable. Significant differences between the theory and data are described. Some models were developed or updated as a result of this study.

2.0 INTRODUCTION

The Rockwell Solid State Photomultiplier (SSPM)[1] is an impurity-band avalanche device which can count individual photons with wavelengths between 0.4 and 28 μm.[2] The response of the SSPM to a photon is a pulse of between 10^4 and 10^5 conduction electrons, making it an important device for use in low-background, near- to mid-IR detection applications. The SSPM is, however, a new device which must be better understood before it is incorporated into an overall system design.

Results of experimental and theoretical work undertaken to better understand and characterize the SSPM for use in astronomy applications are described in this report. Sections 3.0 through 8.0 emphasize results of measurements performed on existing detectors, and presents some equations which can be used to describe the results. Sections 9.0 through 9.4 discuss a model of the SSPM avalanche, and compare some of its implications with an experimentally measured pulse height distribution.

Fig. 1 shows the experimental setup used to measure SSPM characteristics, and Fig. 2 displays typical electronics used in making the measurements.

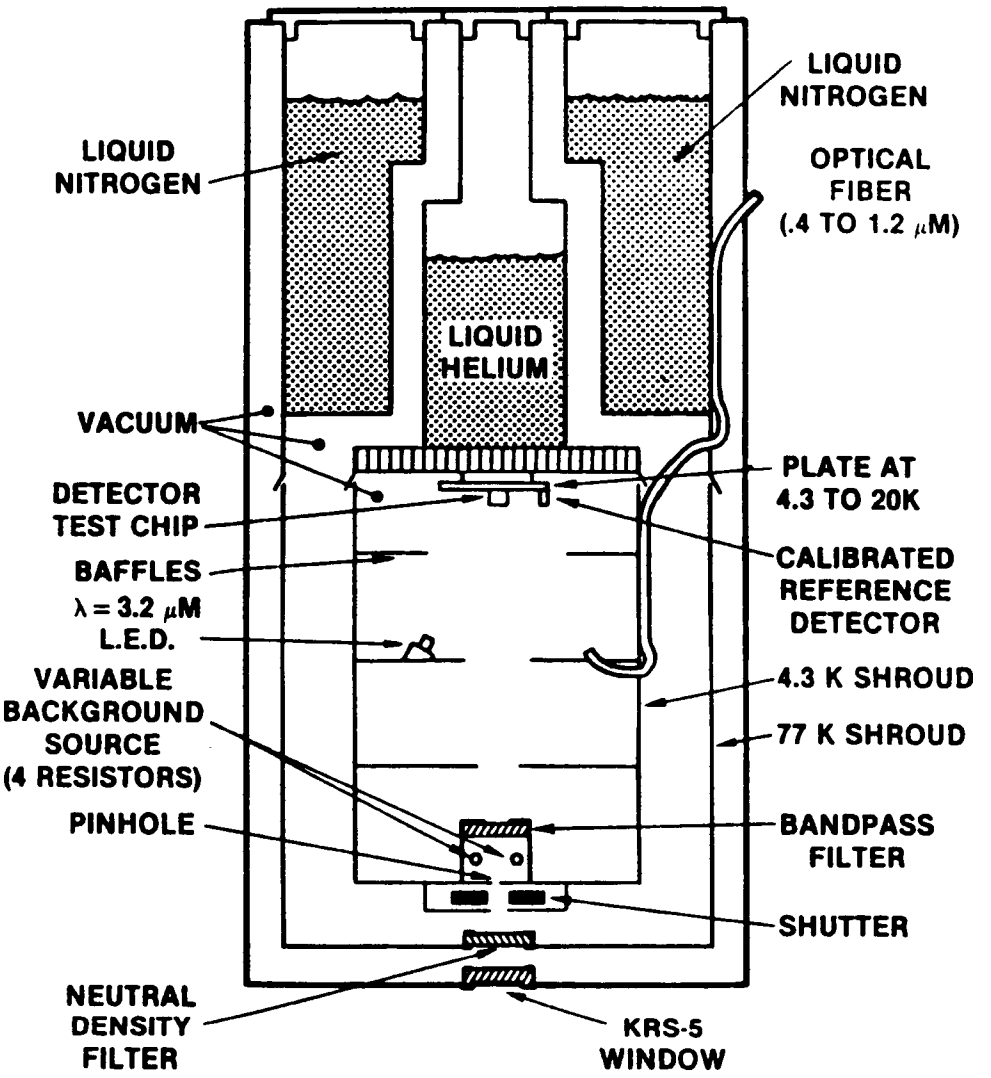

Figure 1. Experimental Setup

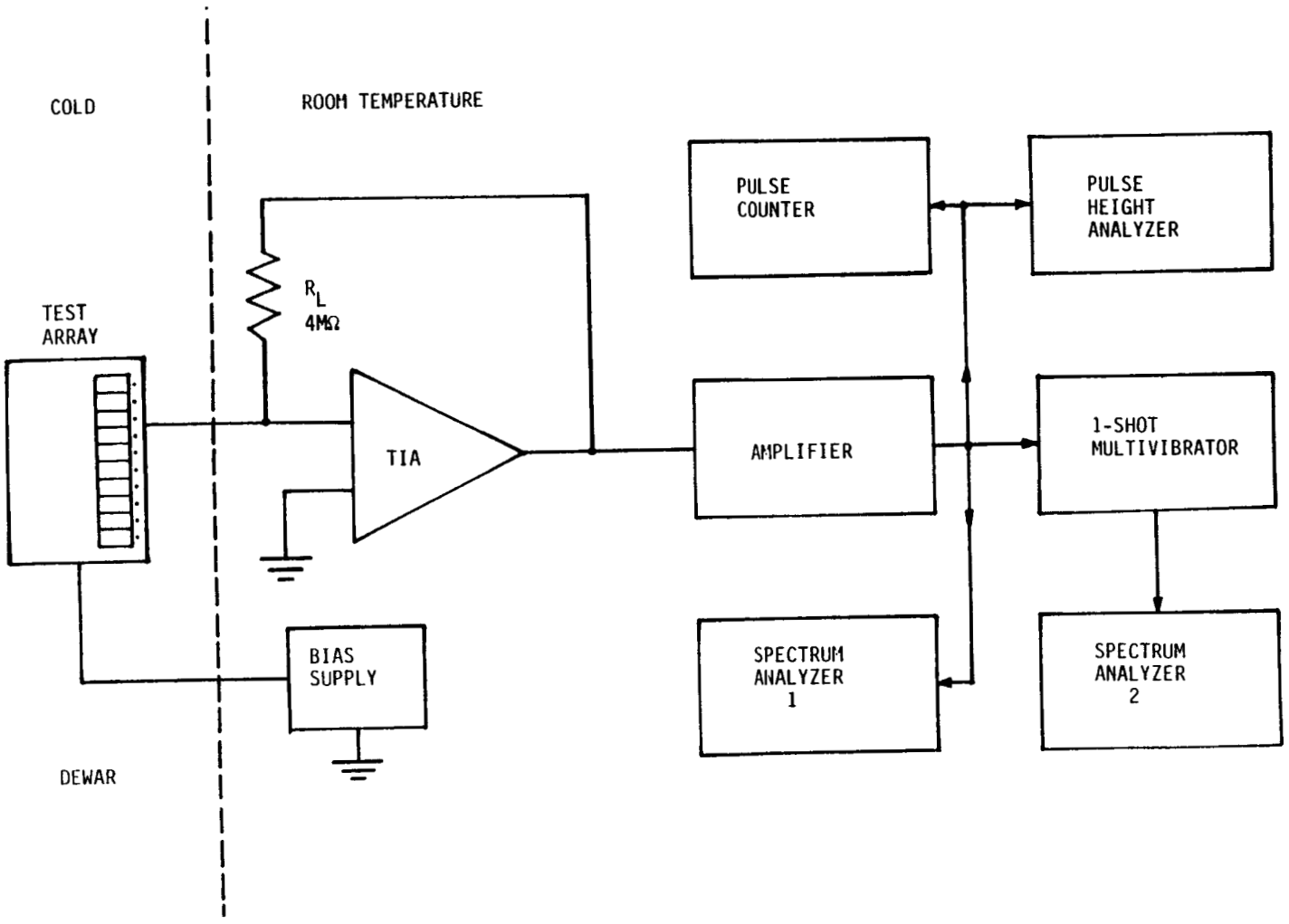

Figure 2. Typical Measuring Electronics

3.0 DARK CURRENT

The dark current (steady-state bias current) varied approximately exponentially with both bias voltage and reciprocal temperature under "zilch" illumination ($<10^6$ photons/cm^2-s). The data shown were taken using an array containing nine 4 x 10 mil^2 pixels. Data were also taken on a 6 x 6 mil^2 discrete detector from the same wafer. The results are shown in Tables I and II, and data from the discrete detector is plotted in Figs. 3 and 4. Bias current is given by

$$I_{bias}(V,T) = C_1 A_{eff} \exp(C_2 V + C_3/T),$$

where A_{eff} is effective detector area and C_1, C_2 and C_3 are constants which depend on the doping levels and profiles used in a particular device. The departure from exponential dependence at lower bias values is due to changes in the electric field profile in the infrared-active region of the detector caused by the doping profile and field-assisted thermal ionization (Poole-Frenkel effect).

It is important to note that, due to the structure of the detector, the carriers responsible for the steady-state bias current were not subject to the full SSPM gain. As a result, the dark current had very low noise, and SSPM pulses due to detected photons or occasional dark counts stood out well above the dark current noise.

At 6.0 K and below, little or no SSPM action was observed; however, at the time of this writing, devices which exhibited SSPM action at lower temperatures were undergoing preliminary testing on another program.

Table I. Bias current as a function of temperature and bias voltage on 4 x 10 mil^2 detectors.

Pixel No.	Temperature(K),Voltage(V) 6,5	6,6	6,7	7,5	7,6	7,7	8,5	8,6	9,5	9,6
1	.245	.827	2.75	1.424	3.81	9.57	4.99	11.90	12.39	27.8
2	.243	.810	2.81	1.420	3.71	9.87	5.01	11.83	12.40	27.8
3	.243	.775	2.65	1.333	3.59	9.25	4.88	11.53	12.12	27.0
4	.227	.774	2.55	1.312	3.55	8.95	4.72	11.24	11.55	26.0
5	.215	.738	2.44	1.280	3.48	8.78	4.67	11.01	11.55	26.1
6	.222	.738	2.41	1.248	3.40	8.55	4.55	10.85	11.29	25.4
7	.216	.727	2.44	1.285	3.45	8.72	4.62	11.08	11.19	25.5
8	.225	.740	2.39	1.280	3.42	8.65	4.52	10.91	11.23	25.4
9	.242	.735	2.40	1.265	3.38	8.56	4.52	10.85	11.28	25.2

Current values are in 10^{-9} A

Table II. Bias current as a function of temperature and bias voltage on a 6 x 6 mil^2 detector.

	Temperature(K)							
V_{bias}(V)	6.0	6.5	7.0	7.5	8.0	8.5	9.0	9.5
4.0	.125	.337	.751	1.553	2.44	4.04	6.00	8.38
4.5	.260	.667	1.425	2.85	4.41	7.14	10.49	14.95
5.0	.495	1.195	2.42	4.71	7.19	11.65	17.85	26.1
5.5	.890	2.01	3.90	7.32	11.25	18.80	28.9	42.3
6.0	1.54	3.24	5.99	11.21	17.63	29.0	44.4	64.5
6.5	2.63	5.10	9.17	17.29	26.9	43.1	65.3	93.8
7.0	4.38	8.11	14.45	26.4	40.1	62.4	93.4	133.3

Current values are in 10^{-9} A

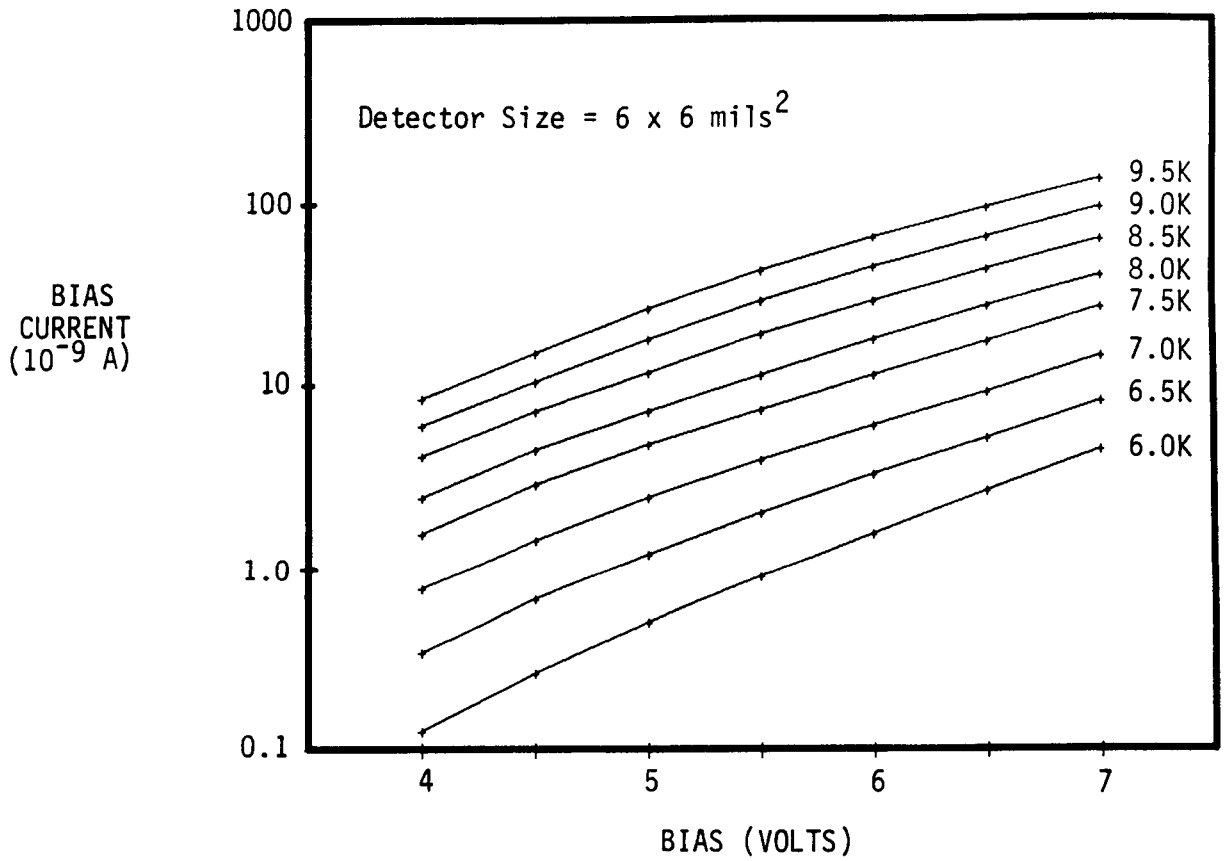

Figure 3. DC Bias Current vs Bias Voltage

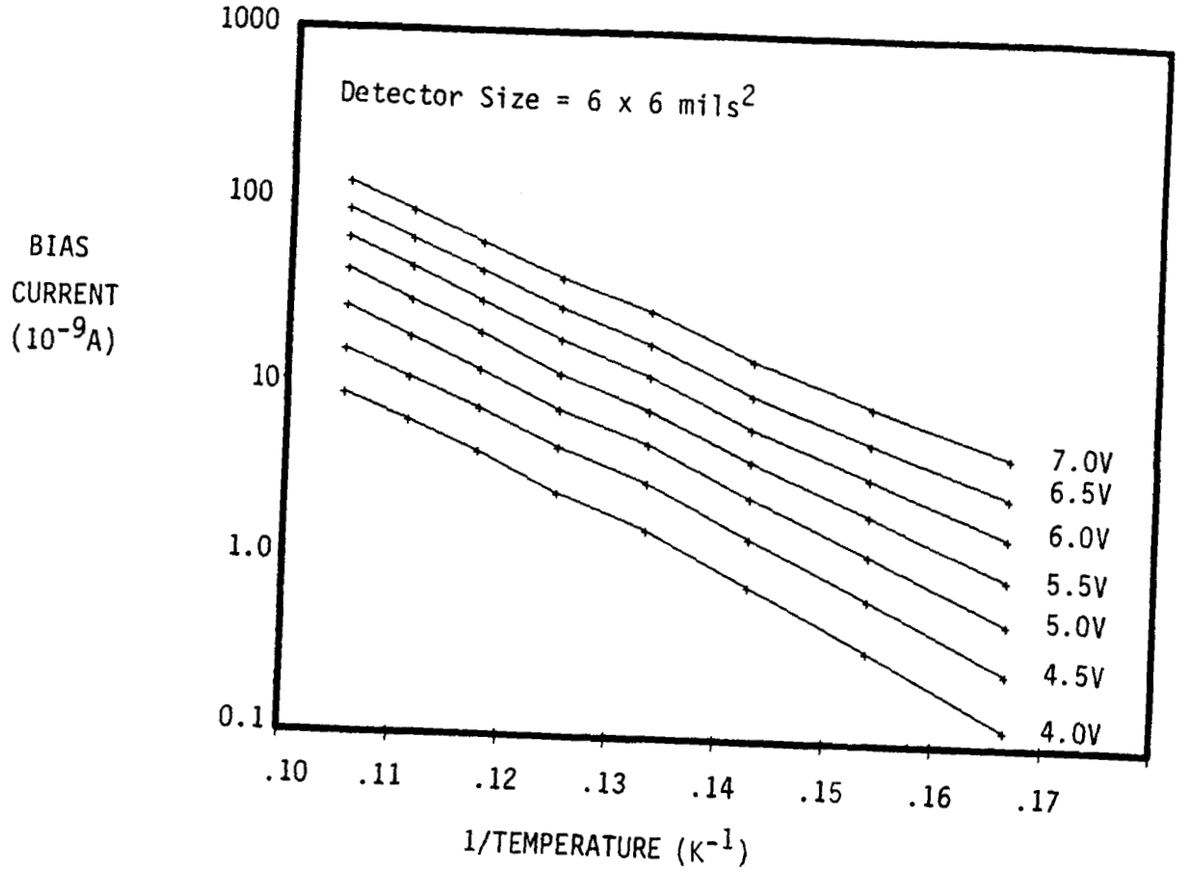

Figure 4. DC Bias Current vs Reciprocal Temperature

4.0 QUANTUM EFFICIENCY AND SPECTRAL RESPONSE

The quantum efficiency and spectral response of SSPMs were measured using front illumination. Fig. 5 shows the counting quantum efficiency of a front-illuminated SSPM in both the infrared and visible regions as a function of wavelength.

Edge-illumination increases the optical path length for photon wavelengths with long attenuation lengths (i.e., wavelengths less than 5 μm), thereby increasing the probability that a photon will be absorbed and improving the quantum efficiency. Fig. 6 shows an example of an experimental geometry used to compare front and edge illumination. Fig. 7 shows the ratio of quantum efficiencies for front- and edge-illuminated SSPMs as a function of incident wavelength. The incident flux density during these measurements was on the order of 10^8 photons/cm^2-s. The ratio of quantum efficiencies was calculated using:

$$R_\eta = \eta_{edge}/\eta_{front} = (A_{front}/A_{edge})f_{edge}/f_{front}$$

where the areas A are effective detector surface areas and the count rates f are given by:

$$f = f_{illuminated} - f_{dark}$$

Assuming that photogenerated electrons in the infrared-active region do not recombine with positive charges before reaching the gain region, the quantum efficiency and attenuation length are related by:

$$\eta = (1-R)[1-\exp(-x/a)],$$

where η is quantum efficiency, R is reflectivity at the detector surface, x is the optical path length and a is the attenuation length for a given wavelength. Therefore, for $a >> x$, $\eta_{edge}/\eta_{front} = x_{edge}/x_{front}$.

For space-based astronomy using wavelengths in the 1 to 5 μm range, edge-illumination should be considered if a discrete device or a line array of detectors is desired, or if the resultant improvement in quantum efficiency justifies the additional effort associated with building an edge-illuminated area array.

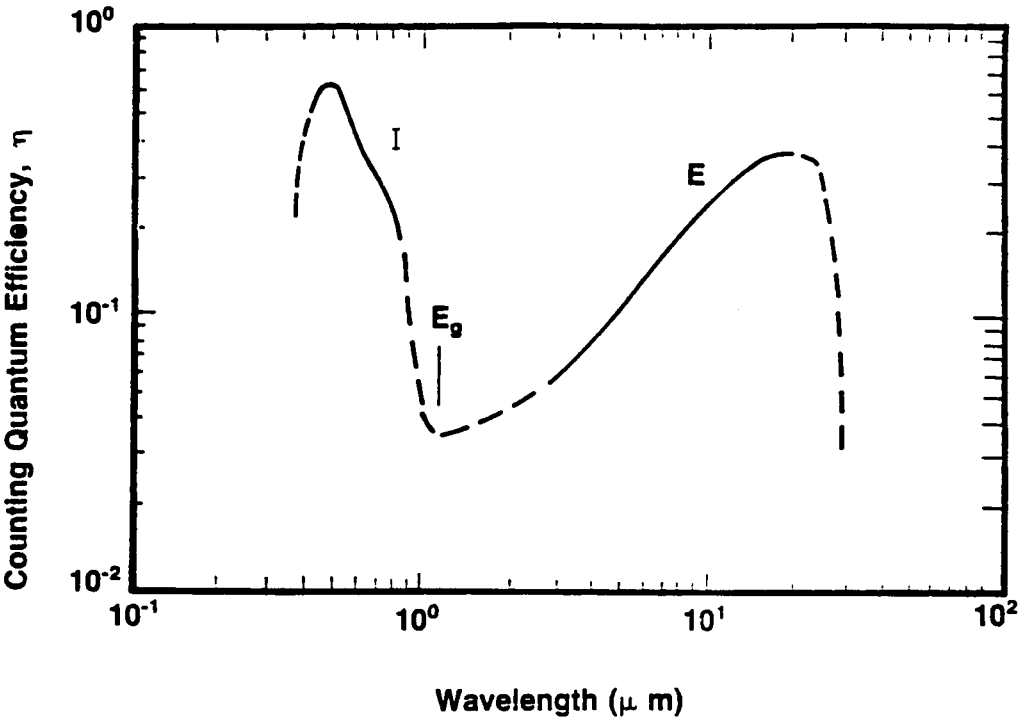

Fig. 5. Spectral dependence of the counting quantum efficiency, η. The solid curves are based on experimental data and the dashed curves are theoretical predictions for intrinsic (I) and extrinsic (E) response. E_g denotes the photon energy corresponding to the silicon bandgap. These curves characterize SSPM performance obtainable at an operating temperature of 7K, with a bias of 7V.

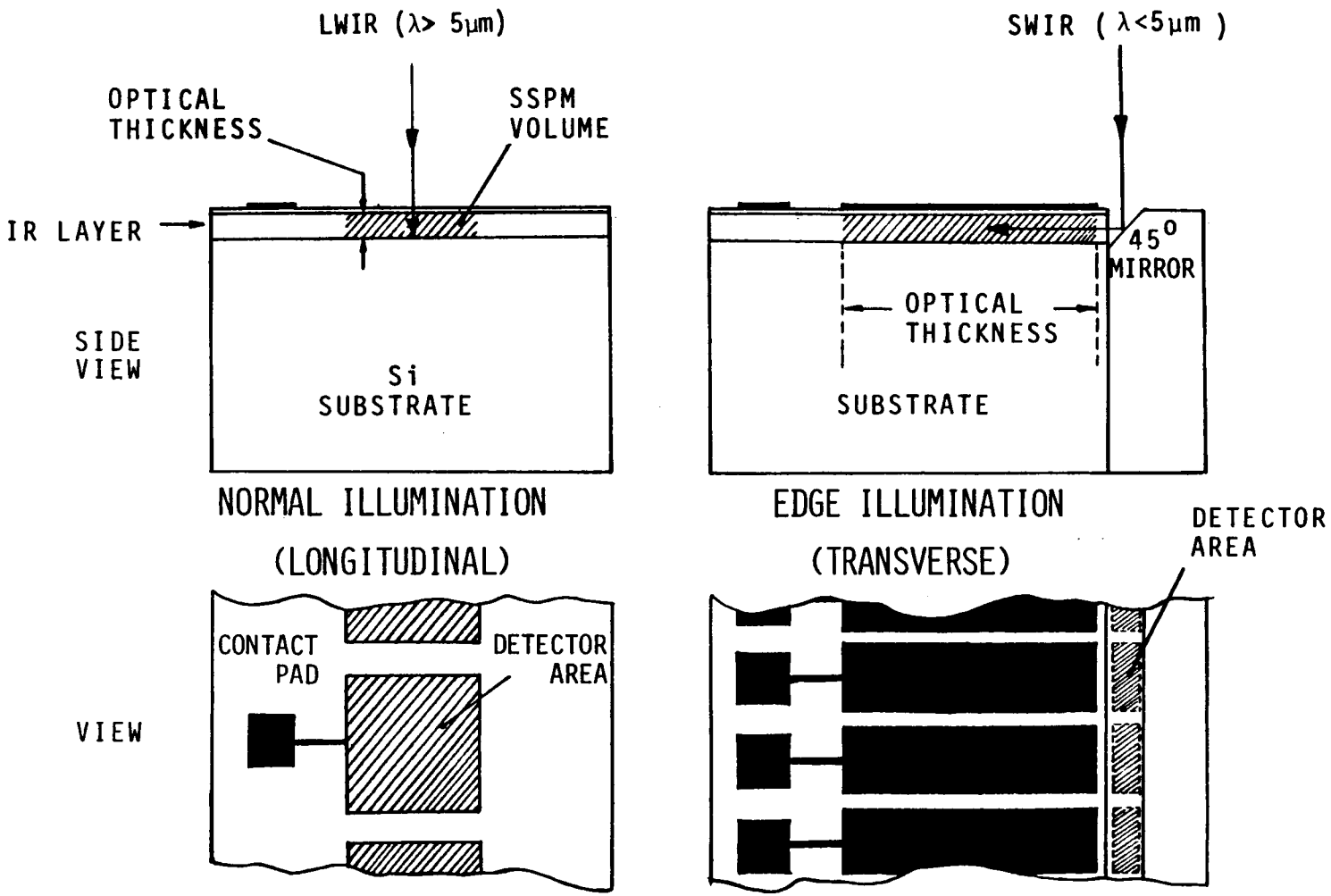

Figure 6. Front and Edge Illumination Geometries

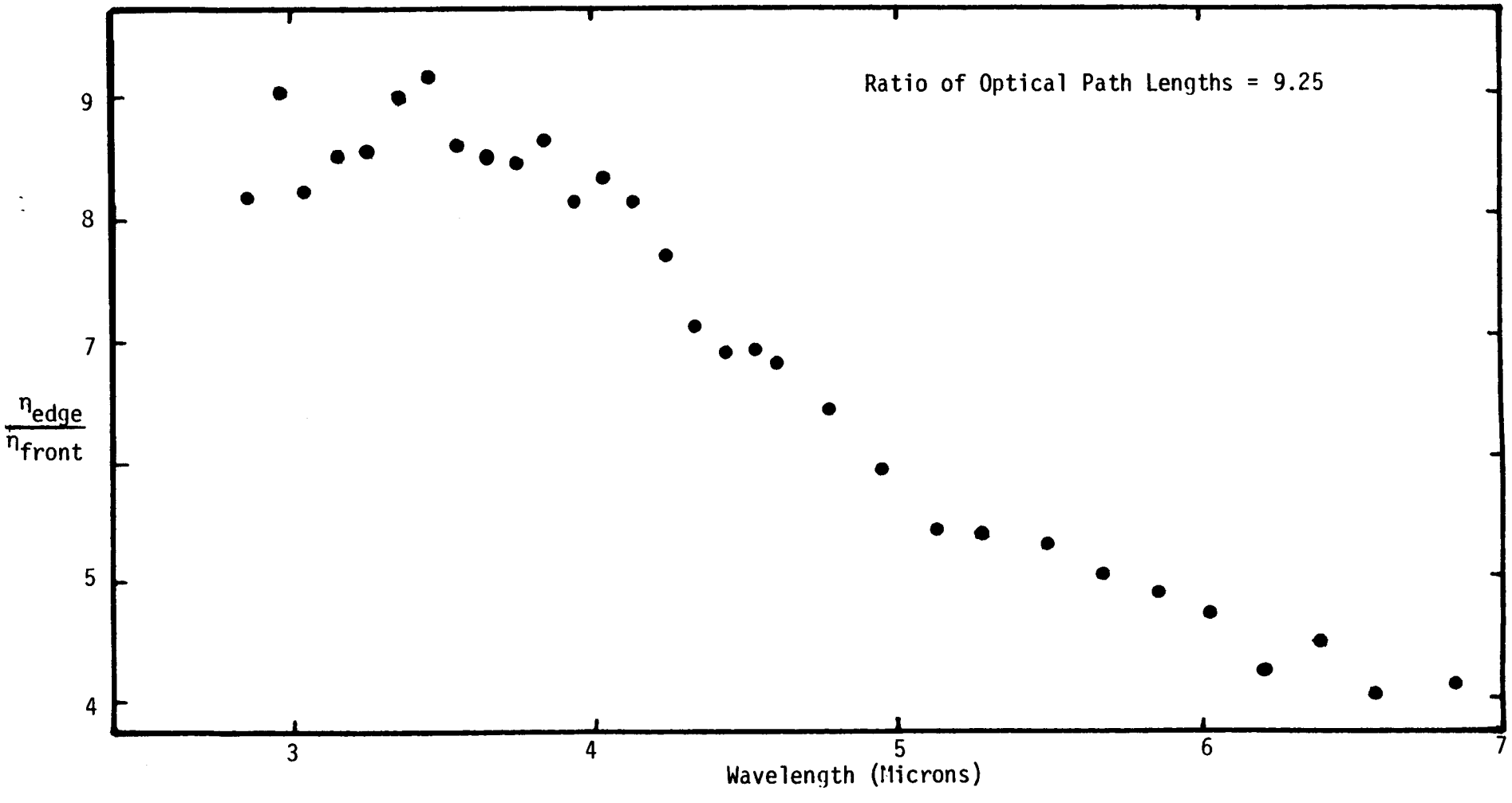

Figure 7. Ratio of Quantum Efficiencies for Edge and Front Illuminated SSPMs vs Wavelength

5.0 ARRAY UNIFORMITY

The uniformity of a 6 x 6 array of detectors was measured at T = 7 K, V_{bias} = 8.3 V, λ = .565 μm. The array is shown in Fig. 8. The test dewar had three leads which were not connected to the test package, so that only 33 of the 36 elements were tested. The pixel area was 6 x 6 $mils^2$, and each pixel was separated from its neighbor by 2 mils. The array contained one anomalous pixel (probably caused by a small defect in the silicon crystal structure) whose quantum efficiency was less than 27%. Results from the remaining pixels are given in Table III.

The quantum efficiencies were calculated from gathered data using:

$$\eta = (f_{illuminated} - f_{dark})/(\Phi A_{pixel})$$

where Φ = 2 x 10^7 photons/cm^2-s. This array was obtained from the most recent lot of SSPMs, and its properties and operating parameters have not yet been fully characterized. For example, higher quantum efficiencies than those reported in Table III are currently being obtained under other conditions.

Table III. Quantum efficiency of pixels in a 6 x 6 SSPM array. The array is shown in Fig. 8. Each pixel was 6 x 6 mils^2, and was separated from its neighbors by 2 mils. Measurements were taken using V_{bias} = 8.3 V, T = 7 K, Φ = 2 x 10^7 photons/cm^2-s, λ = .565 μm.

Pixel	η(%)	Pixel	η(%)	Pixel	η(%)
1	46.1	12	45.6	23	46.2
2	48.3	13	46.1	24	47.1
3	46.7	14	46.9	25	45.1
4	44.4	15	44.6	26	47.6
5	45.6	16	45.6	27	46.7
6	45.8	17	43.1	28	44.7
7	42.8	18	46.1	29	44.7
8	45.9	19	46.2	30	43.3
9	45.8	20	47.2	31	45.3
10	47.2	21	46.1	32	44.1
11	46.7	22	46.0		

Average η = 45.7 ± 1.3% over 32 pixels

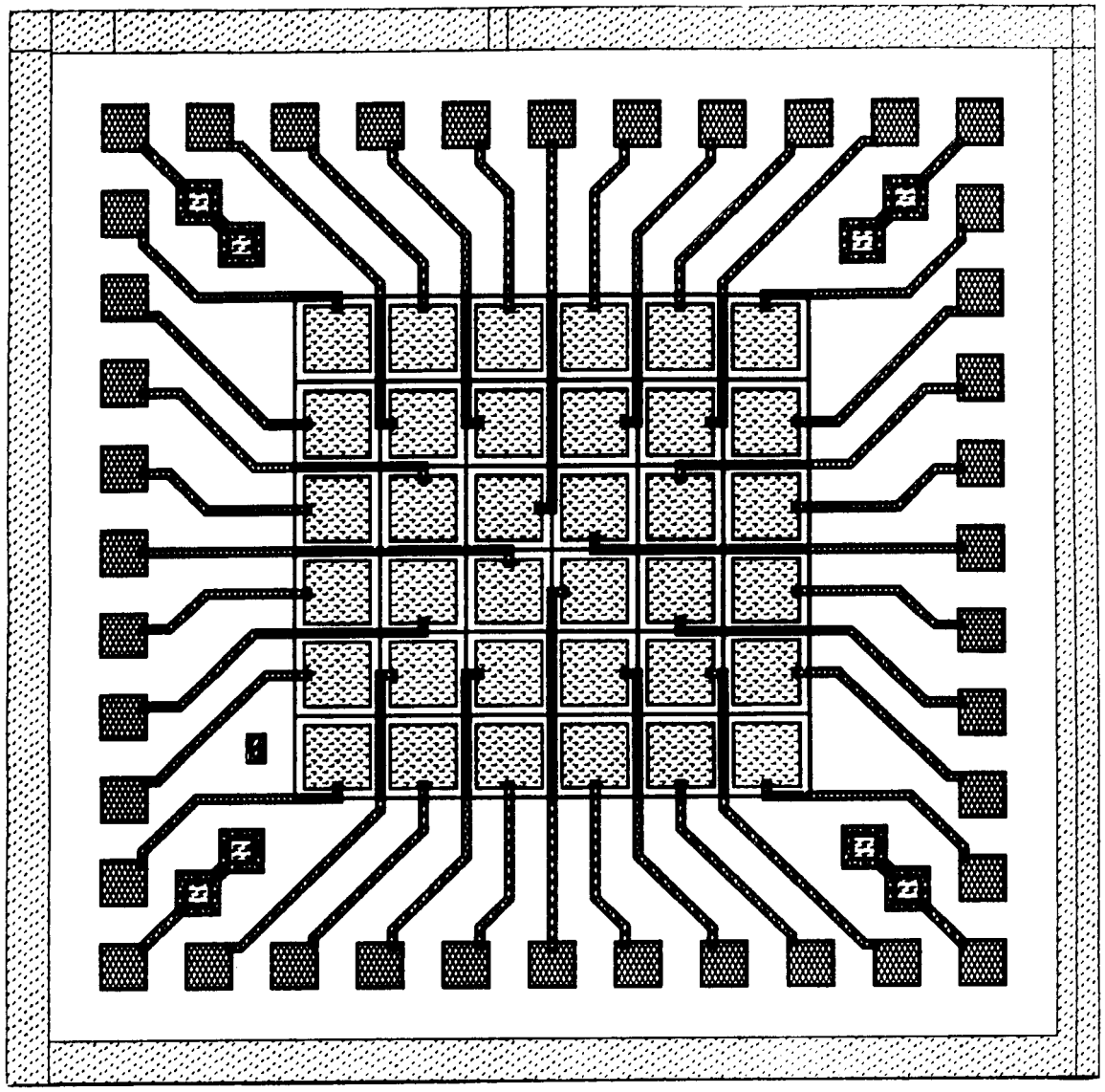

Figure 8. 6 x 6 SSPM Array

6.0 DARK COUNTS AND SATURATION

The dark count rate of an SSPM varied approximately exponentially with temperature for temperatures up to about 9 K. Saturation occurs because time is required to sweep D^+ charges out of the detector's infrared active layer following production of a photon pulse and re-establish the electric field profile required for proper SSPM action. The disturbance in the electric field caused by the D^+ charges creates a circular dead zone at the surface of the (front-illuminated) detector, within which subsequent incident infrared photons will produce pulses of diminished amplitude until the electric field profile is re-established. The required dead time diminished with increased temperature, but had a somewhat weaker dependence than the dark count rate, so that the detector's dynamic range depended on temperature. At temperatures near 10 K, the dark count rate approached the saturation count rate, so that the dynamic range of the device diminished. This is illustrated by the graph shown in Fig. 9.

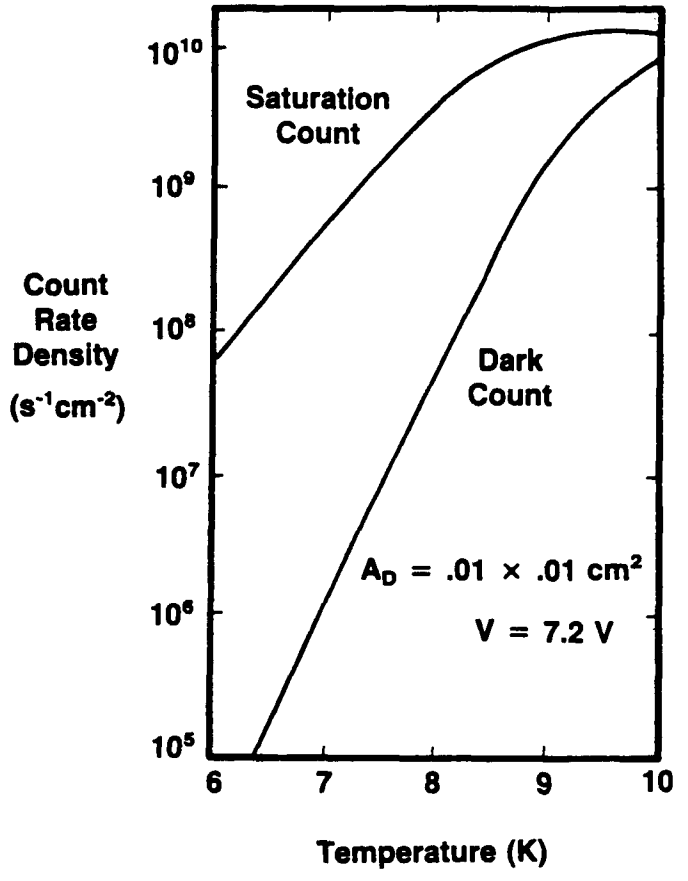

Figure 9. Temperature dependence of the SSPM dark count rate and saturation count rate densities.

7.0 NOISE

Measurements showed typical 1/f noise, due to amplifier noise and small fluctuations in the bias current. This noise could be eliminated by counting photon pulses above a set threshold (e.g., by triggering a one-shot with the SSPM photon pulses). Fig. 10 shows the frequency response, in both direct and one-shot modes, of an SSPM which was exposed to infrared pulses at a rate of about 150 Hz. The 1/f noise evident in direct mode was drastically reduced in one-shot mode.

SSPM dark pulses were uncorrelated in time. Therefore, in one-shot mode, the noise associated with the device was pure shot noise associated with the average dark pulse rate.

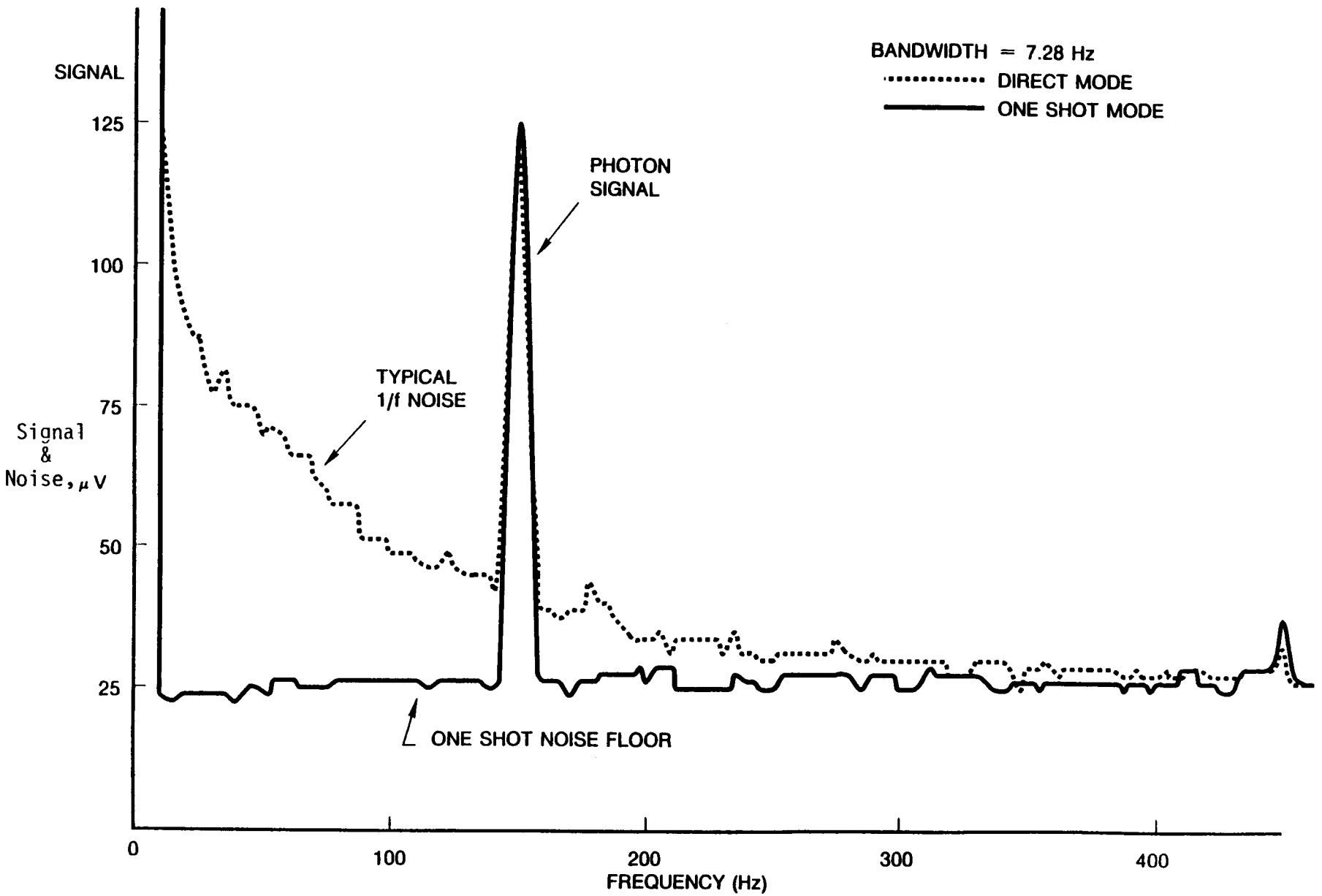

Figure 10. SSPM signal and noise vs frequency

8.0 SUGGESTED OPERATING CONDITIONS

In order to maximize the SSPM's dynamic range, the device should be operated at the low end of the usable temperature range. For the devices characterized in this study, the recommended operating temperature is 7 K. To maximize quantum efficiency at this temperature, the highest bias voltage that can be applied without a significant risk of overloading the device is 7.0 V.

Since these detectors function as high-impedance devices that emit sharp current pulses, their outputs should first be processed through a transimpedance preamplifier. Care should be taken to keep stray capacitance between the SSPM and the preamplifier below a few tens of picofarads in order to avoid attenuating the SSPM pulse amplitudes.

9.0 PHENOMENOLOGICAL MODEL OF SSPM AVALANCHE GAIN STATISTICS

9.1 Background

The Rockwell Solid State Photomultiplier (SSPM)[1] is an impurity-band avalanche device which can count individual photons with wavelengths between 0.4 and 28 μm.[2] The response of the SSPM to a photon is a pulse of between 10^4 and 10^5 conduction electrons. The photon initiates an avalanche of electrons through the photoionization of a single impurity, one of many found in a region of high impurity concentration in the device. The released electron is subsequently accelerated by an external electrical field until it ionizes another neutral impurity atom. The resulting pair of electrons are in turn accelerated until they impact-ionize other neutral impurities, and in this way an avalanche of conducting electrons develops in the region of high impurity concentration. In this report, a new phenomenological model of the avalanche process in the SSPM is discussed. The model reproduces, with a few physical and empirical assumptions, the important and peculiar features of the distribution h(n) of the number (n) of electrons in a pulse. The pulse distribution h represents the fluctuations in the population of the pulses, and therefore contains valuable information about both the performance of the SSPM and the underlying mechanisms crucial to that performance.

The observed h(n), shown in Fig. 11, is remarkable in several respects. First, the gain $\langle n \rangle$, where

$\langle n \rangle$ is estimated by $\sum_{n=1} nh(n)$,

(h(n) is normalized throughout this work), is enormous, ranging from 10,000 to 50,000 for the devices produced so far. The mechanisms directly responsible for such large gains are not well understood and will be addressed only indirectly in this work. Instead, this report speaks directly to a second outstanding feature of h(n), namely, its narrow peak near the gain, and the resulting small gain dispersion $\sigma \leq \langle n \rangle/2$,

where σ^2 is estimated by $\sum_{n=1} (n-\langle n \rangle)^2 h(n)$.

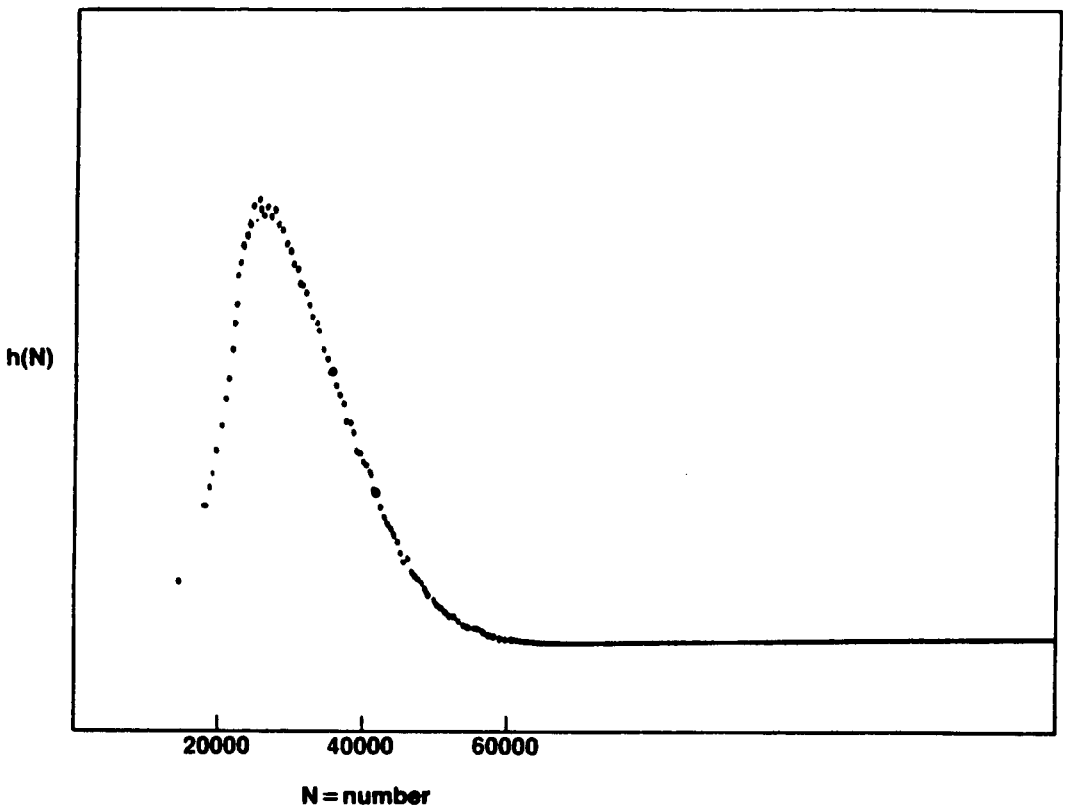

Figure 11. Observed SSPM pulse distribution. See Table V for statistical attributes.

In order to appreciate the peculiarity of the shape of h(n), the observed h(n) is shown in the next section (9.2), to be incompatible with the traditional descriptions of the avalanche process as applied to other devices, e.g., avalanche photodiodes. This incompatibility motivates the subsequent development in section 9.3 of a new phenomenological description of the avalanche process developed along the lines of classical mathematical theory of branching, and the results are explained in section 9.4. Finally, in section 9.5, the implications of the new model for the future modeling and design of the SSPM are discussed.

9.2 Conventional (Markov) Description of the Avalanche Process

In the usual treatments of, e.g., avalanche photodiodes, h(n) is calculated from a phenomenological rate α, i.e., the number of electrons generated per unit distance.[3] Usually (and apparently exclusively) α is described as varying only with the position t of a carrier, usually in one dimension, along a line antiparallel to the field. Since $\alpha(t)$ is independent of the history of a carrier, this description requires that the avalanche develop as a Markov process. If in addition the carriers do not interact with each other (and they do not in traditional treatments), the avalanche may be described by the classical theory of branching.[4][5] In particular, the theory yields p(n,t;m), i.e., the probability that at t there are n carriers given m carriers at the origin. In what follows, position is written in reduced units so that the end of the avalanche region is at t=1, and its origin is t=0. For a photon counting device, $h(n) \equiv p(n,1;1)$.

The calculation of p(n,t;m) for a Markov branching process in one dimension follows immediately, with only the following additional assumptions. First, only one type of carrier is considered here, since in the SSPM only one type of carrier is effectively mobile during the lifetime of one avalanche; for other devices,where the mobile carriers are, respectively, electrons and holes, two-type branching processes are easily discussed.[3] Second, the carriers do not recombine or otherwise disappear. Third, upon impact-ionization of a neutral impurity, the original carrier "dies" and simultaneously exactly two carriers are "born". Then, for any continuous $\alpha(t)$, p must satisfy the following differential equations[4][5]

$$\frac{dp(n,t;m)}{dt} = -n\alpha(t)p(n,t;m) + (n-1)\alpha(t)p(n-1,t;m), \qquad (9.2.1)$$

$$\frac{dp(m,t;m)}{dt} = -m\alpha(t)p(m,t;m),$$

with the initial conditions $p(m,0;m) = 1$, $p(n,0;m) = 0$, and $n>m\geq 1$. The solution is

$$p(n,t;m) = \left(\frac{n-1}{n-m}\right)(q_t-1)^{-m}(1-1/q_t)^n, \text{ where } q_t = \exp\int_0^t ds\ \alpha(s).$$

The gain, as a function of position, is $\langle n(t)\rangle = mq_t$. For both large n and m, $p(n,1;m,0)$ is a unimodal function with its peak near the mean, and indeed, avalanche photodiodes frequently display such a distribution of pulse populations. However, this behavior depends upon the fact that avalanche photodiodes do not continuously count single photons, but instead respond to pulses of photons ($m \geq 200$). In the photon counting mode, m must be unity, and the resulting distribution would be

$$h(n) \equiv p(n,1;1) = (1-1/q_t)^n/(q_t-1), \qquad (9.2.2)$$

a monotonically decaying function with $\langle n\rangle = q_t$, far from the peak at n = 1. Nevertheless, Fig. 11 shows that the observed h(n) is a unimodal function with its peak near the mean.

Before rejecting the Markov branching hypothesis, it should be noted that there is a type of Markov branching process which (for m = 1) may produce a unimodal function decreasing on both sides, namely, the multiple-stage process.[4][6] Such a process could apply to the venerable photomultiplier tube,[7] where the multiplication occurs in discrete stages. Although peaked pulse height distributions usually are not observed for photomultiplier tubes,[7] Capasso[3] has apparently constructed a solid-state analogue to the multiple-stage photomultiplier tube which displays such a peaked h(n). The number distribution is apparently well described by the multiple-stage Markov process for his device. However, such considerations are inapplicable to the Rockwell SSPM, since it does not possess a multiple-stage structure. Therefore, a model compatible with the observed h(n) must reject either the neglect of carrier-carrier interactions, the Markov hypothesis, or both.

The effect of carrier-carrier interactions could be to cut off the avalanche as a critical number of carriers is exceeded in each pulse. This could happen if a large number of carriers are so concentrated (in space) in the avalanche that the corresponding dense configuration of ionized impurities screens the electric field, thereby reducing the acceleration of the carriers and hence the probability of further impact ionization of neutral impurities. A sharply peaked h(n) could result from this proposed screening. In the context of Markov processes, this would require that α depends both on t and n(t), the instantaneous number of carriers at t. Although still Markovian, the avalanche could no longer be described by a classical branching process. However, if the interactions are not too strong or rapidly varying, such a process could be simulated by way of the Boltzmann transport equation.[8] This screening scenario requires the production of both large gains and dense (in space) pulses of carriers in the SSPM; apparently the pulses must approach near-plasma densities to induce screening. While this scenario is plausible for devices where the gain is at least as large as 50,000, for similar devices with lower gains, e.g., 15,000 (shown in Fig. 11), this mechanism should not be expected to operate alone, if at all. On the other hand, if carrier-carrier interactions may be neglected, i.e., α is independent of n, then the Markov assumption must be certainly rejected. The focus in the next section is on the development of a non-Markov (history-dependent) model of the avalanche for non-interacting carriers. Table IV summarizes the dependency of α for the variety of hypotheses just mentioned.

9.3 A Non-Markov Phenomenological Model of the Avalanche

By rejecting the Markov assumption, the branching rate α must depend on the history of a carrier as well as, if at all, upon its position. The importance of the history of an avalanching carrier in the SSPM is indicated by the following consideration of impact ionization. First, impact ionization of neutral impurities occurs only when the colliding carrier attains or surpasses a critical energy. Contrary to the Markov assumption, the carrier does not attain the critical energy instantaneously, but must be accelerated by the applied field over a critical distance x_c from its origin. In fact, in what follows, all carriers created by impact ionization will be assumed to initially possess zero energy, so that all the energy gain is due to the field alone.

Table IV. Dependency of α upon position t, distance x, and number of carriers n for six hypotheses.

	HF	IF	IF+CC
Markov	α	$\alpha(t)$	$\alpha(n,t)$
Non-Markov	$\alpha(x)$	$\alpha(t,x)$	$\alpha(n,t,x)$

HF: Homogeneous Field
IF: Inhomogeneous Field
IF+CC: Inhomogeneous Field with Interacting Carriers

Further, the scattering of sub-critical carriers by phonons and neutral impurities, respectively, will induce a distribution of critical distances which a carrier must traverse from its origin to attain the critical energy for impact ionization. Finally, after reaching the critical energy, the carrier must traverse another distance before colliding with a neutral impurity. Since the impurities are randomly dispersed in the avalanche region, an additional distribution of critical distances is introduced. Let $\rho(x)$ represent the cumulative probability that a neutral impurity is found on the line x beginning at the origin. Then, writing the normalized distance distribution $f = f(x,t)$ to indicate its dependence on both the position t of the carrier and the distance x traveled from its origin, the non-Markovian branching rate $\alpha(t,x)$ is the convolution[9]

$$\alpha(t,x) = r\int_0^x dy\ f(y,t)\rho(x-y), \qquad (9.3.1)$$

where r is an effective constant branching rate. The impurity distribution[10] is found immediately to be $\rho(x) = 1-\exp(-cx)$, where $c = \gamma n_I$ and n_I is the concentration of impurities and γ is the effective cross-section. Since both position and distance are dimensionless in this work, x is scaled by the distance of the avalanche region, which for the SSPM is taken to be 4×10^{-4} cm. Typical values* for the SSPM are $n_I = 5\times10^{17}$ cm^{-3} and $\gamma = 1.6\times10^{-13}$ cm^2, so that for the reduced distances ($0 \le x, t \le 1$), $c = 32$. The Markov branching rate $\alpha(t)$ is recovered only when f factorizes as $f(x,t) = \Phi(t)\delta(x)$, where δ is the Dirac delta function, and also as $c \to \infty$. It remains to develop a model for $f(x,t)$ and the branching equations for $p(n,t;1)$.

It is convenient to develop f for the case of a homogenous electric field, although the field in the SSPM is more nearly linear. For the homogeneous field, f is independent of position. The probability that a carrier first attains the critical energy is zero before the minimum critical distance x_c. This distance is determined solely by the field, and represents the critical distance required in the absence of scattering. Thus f(x) factors as $H(x-x_c)g(x-x_c)$, where $g(y<0) = 0$, and H(x) is the unit step function centered at the origin. The normalized function g therefore represents the effect of scattering, which slows down the carriers and so randomly increases the critical distance.

---

*The cross section (c.g.s.) is approximated by $\gamma = \pi(e^2/\varepsilon E_{min})^2$. For arsenic-doped silicon, $E_{min} = 55$ meV and $\varepsilon = 11.4$.

In the absence of scattering, g becomes the Dirac delta function. The simplest model for scattering, by analogy to Shockley's model for photon scattering of carriers,[111] is

$$g(x) = \exp(-x/w)/w$$

where w is a measure of the scattering strength. The mean critical distance $\langle x_c \rangle$ is then $x_c + w$. Therefore, the probability for a carrier to attain exactly the critical impact ionization energy after traveling a distance x from its origin is given by the probability distribution,

$$f(x>x_c) = \exp(-(x-x_c)/(\langle x_c \rangle - x_c)), \text{ with}$$

$$\langle x_c \rangle > x_c \text{ and } f(x<x_c) = 0.$$

For this choice of f, $\alpha(x)$ becomes, after performing the convolution indicated by Eq. 9.3.1.

$$\alpha(x)/r = 1-f(x) - \exp(-c(x-x_c))(1/(1-c(\langle x_c \rangle - x_c))-f(x)).$$

Both f and α are shown in Fig. 12 for $x_c = 0.025$, $\langle x_c \rangle = 0.05$, $c = 32$, and $r = 30$. While the constant c is chosen, as discussed above, to be compatible with the physical parameters of the SSPM, the choice of the remaining parameters represents a compromise between realism and computational convenience. The discussion of these choices is postponed until section 9.4, after the presentation of the equations for p(n,t;1) is complete.

In the model described above, an inhomogeneous field would induce a position dependence in x_c, $\langle x_c \rangle$, and possibly r as well. As the field increases with position, which it does in the SSPM, x_c and $\langle x_c \rangle$ should become smaller, although constraints upon the variation of the ratio $x_c/\langle x_c \rangle$ are unknown. Such refinements of the model should not be pursued until the homogeneous case is better understood. These refinements could in principle be made by way of a microscopic simulation via the Boltzmann equation for non-branching trajectories of the carriers in the SSPM. However, with the expectation that the variation with position of x_c, $\langle x_c \rangle$, and r with position is weak and will not substantially affect the qualitative conclusions, the equations for p(n,t;1) are presented and solved below for the homogeneous field. The equations which lead to h(n) for history-dependent branching are more complicated then those for Markov branching, and do not readily yield an analytic solution.

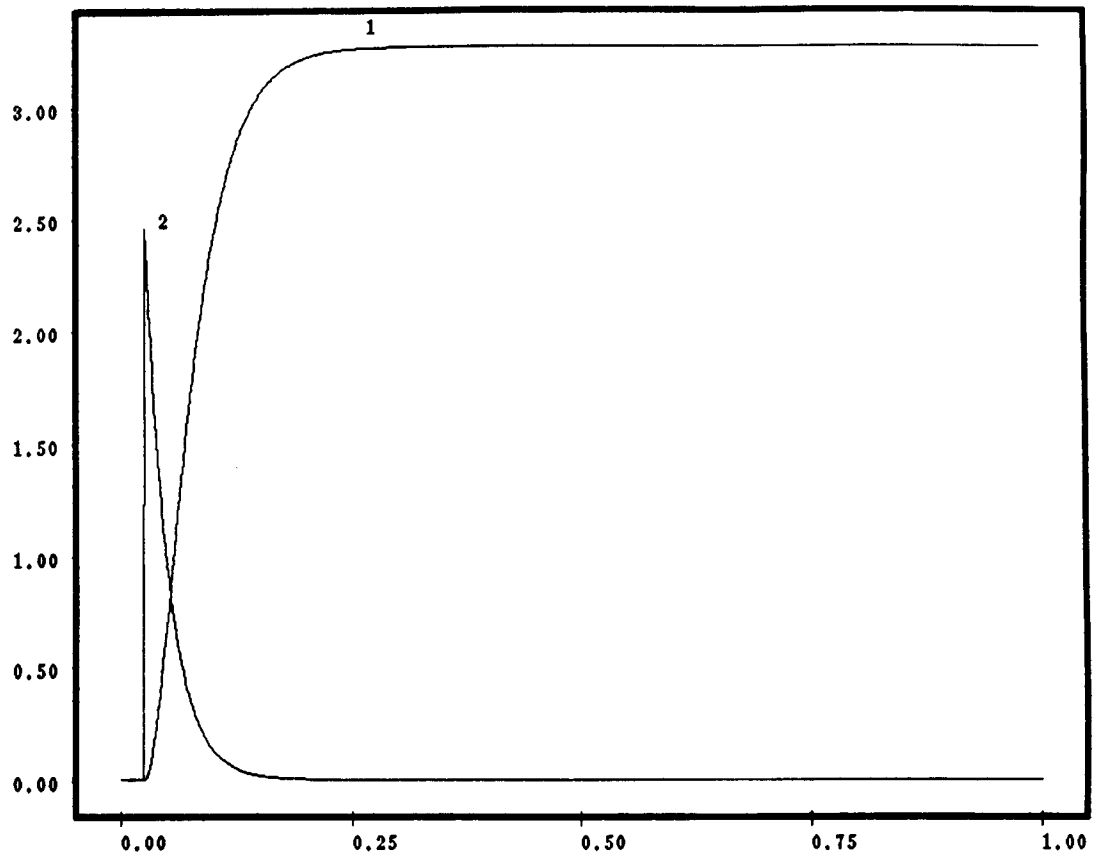

Figure 12. Curve 1 shows $\alpha(x)/100$ and curve 2 shows $f(x)*100$ for $x_c = 0.025$ and $\langle x_c \rangle = 0.050$. The horizontal axis is the scaled distance x.

The equations are greatly simplified for homogeneous fields, where α is independent of absolute position, and may be found in standard texts,[4][12] as reproduced below, namely, for $n > 1$,

$$p(n,t;1) = -\int_0^t dx\ w'(t-x)p^{**}(n;1), \qquad (9.3.2)$$

where $w(t) \equiv p(1,t;1) = \exp(-\int_0^t dx\ \alpha(x))$, $w' = -\alpha w$, and

$$p^{**}(n,t;1) \equiv \sum_{k=1}^{n-1} p(k,t;1)p(n-k,t;1),$$

with the usual initial conditions $p(0,t;1) = 0$ and $p(1,0;1) = 1$. A Markov equation (Eq. 9.2.1) is recovered directly when α is constant. Since the equations above usually require a numerical solution, it is useful to have a check on the results. One test compares the sum

$$\sum_{n=1} p(n,t;1)$$

with unity; the computed difference was always less than 2%. Another, more demanding, test compares the gain calculated as the first moment of p, and independently from the equation for gain, namely

$$\langle n(t)\rangle = w(t) - 2\int_0^t dx\ w'(t-x)\langle n(x)\rangle. \qquad (9.3.3)$$

Comparison between these two mathematically equivalent but numerically distinct equations always revealed less than a 5% difference in $\langle n(t)\rangle$ throughout the range $0<t<1$. A final check on both the numerical and conceptual aspects is provided by the calculation of the combinatorial entropy

$$S(t) \equiv -\sum_{n=1} p(n,t;1)\ \log\ (p(n,t;1)).$$

The entropy is expected and was found to be monotonically increasing throughout the range of t; more than one spurious result was detected with this test.

The lifetime of the first carrier w(t), and the gain $\langle n(t)\rangle$, are displayed in Figs. 13 and 14, respectively, for the parameters $x_c = 0.025$, $\langle x_c\rangle = 0.050$, and $r = 30$. Fig. 13 includes a comparison of w(t) with $\exp(-r_{eff}\ t)$, which would be the corresponding Markov result.

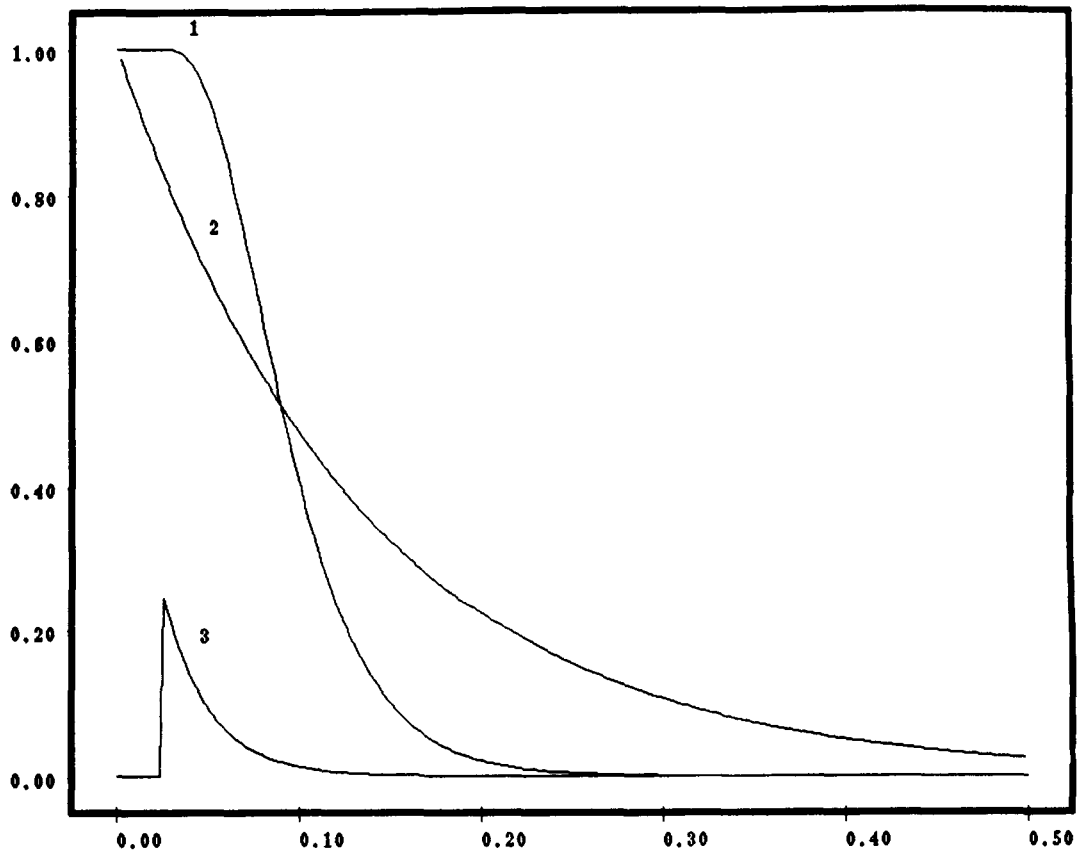

Figure 13. Curve 1 shows the computed w(x) for the non-Markov process (Eq. 9.3.2 in text). Curve 2 shows the corresponding Markov $w(x) = \exp(-r_{eff}x)$, where $r_{eff}=7.51$. Curve 3 shows f(x)*10 for comparison. Other parameters as in Figure 12.

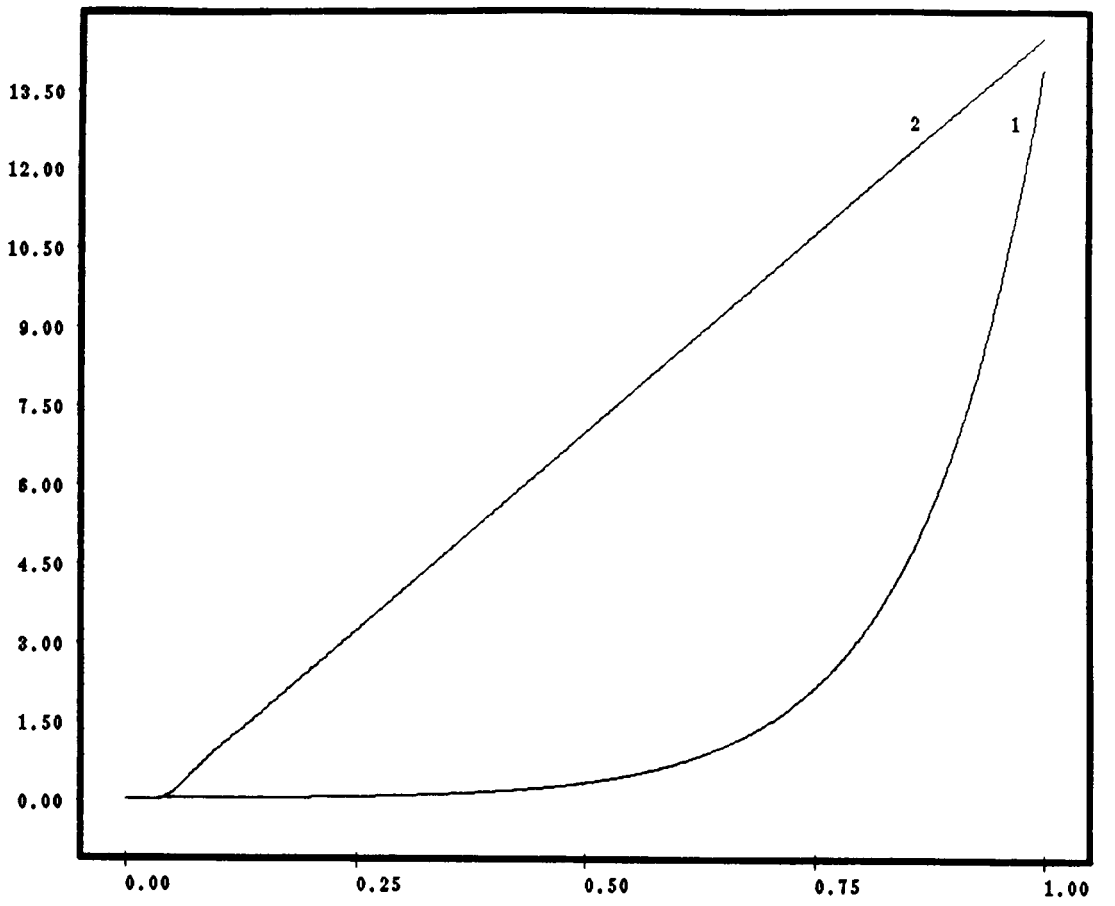

Figure 14. Curve 1 shows the gain (divided by 100) as a function of position. Curve 2 shows twice the log gain. Parameters as in Figure 12.

The coefficient r_{eff} is calculated from $d\log\langle n(t)\rangle/dt\,|_{t=1}$, which would be an exact correspondence if the branching were Markovian. It is interesting to note that for r = 30, r_{eff} = 7.51, thereby indicating how the introduction of relatively small carrier scattering and other history-dependent effects dramatically suppresses the net growth of the avalanche. As required by the asymptotic development of Eq. 9.3.3 for any continuous α, $\langle n(t)\rangle$ is indeed asymptotically exponential in t, as shown in Fig. 14.

Fig. 15 displays the principal result of the calculation of the solution of Eq. 10.2 for x_c = 0.025, $\langle x_c\rangle$ = 0.050, and r = 30, namely, h(n) = p(n,t;1) for t = 0.985 (Fig. 16 is its logarithm). For comparison, the corresponding Markov result (Eq. 9.2.2), is

$$h(n) = (\langle n\rangle - 1)^{-1}\,(1 - 1/\langle n\rangle)^{n},$$

also shown. Comparison with the observed h(n) in Fig. 11 reveals, a strong qualitative resemblance between the observed h(n) and the one calculated for this model, despite the difference in scales. The difference in scales is deferred to the following section.

Fig. 17 shows the development of the pulse distribution as a function of position, namely, p(n,t;1) recorded for t at 0.800, 0.900, and 0.985. As expected, the most drastic changes occur in the latter stages of the avalanche. In fact, for the greater part of the growth of the avalanche, p(n,t;1) more nearly resembles the exponential distribution expected from a Markov process; the influence of the history-dependence is fully manifest only in the latter stages (t > 0.8) of the avalanche. Table V records various statistical attributes of both the observed and the calculated distributions shown in Fig. 17 namely, the gain $\langle n\rangle$, dispersion σ, the mode n_{max} (where the distribution attains the maximum), and the skew κ_1 and the kuritosis κ_2, respectively. The importance of these quantities will be evident during the discussion of the attempts to fit h(n) to known distributions.

Table V. Statistical attributes of calculated and observed h(n)

t	0.7	0.8	0.9	0.985	Observed
n_{max}	127	269	568	1086	30000 ± 5000*
$\langle n \rangle$	144.6	306.4	650.6	1249	35000 ± 5000*
$\sigma/\langle n \rangle$	0.378	0.378	0.378	0.377	0.26
κ_1	0.606	0.595	0.570	0.525	0.4
κ_2	0.49	0.47	0.44	0.38	-

*These values are sensitive to operating temperature and bias.

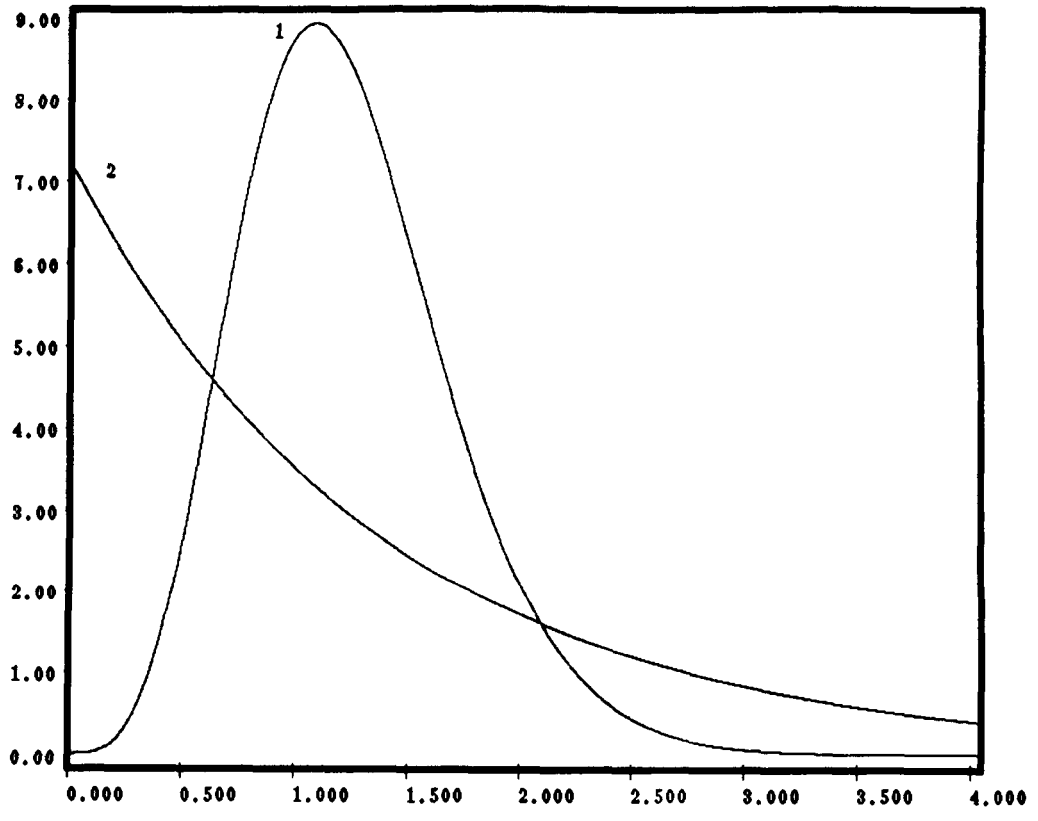

Figure 15. Pulse distributions computed for the non-Markov process (curve 1) and the Markov process (curve 2). The horizontal axis is n/1000, the vertical axis is multiplied by 10^4. Curve 1 is p(n,t=0.985;1), calculated from 9.3.2 and the parameters in Figure 12. Curve 2 is calculated to match the gain for curve 1.

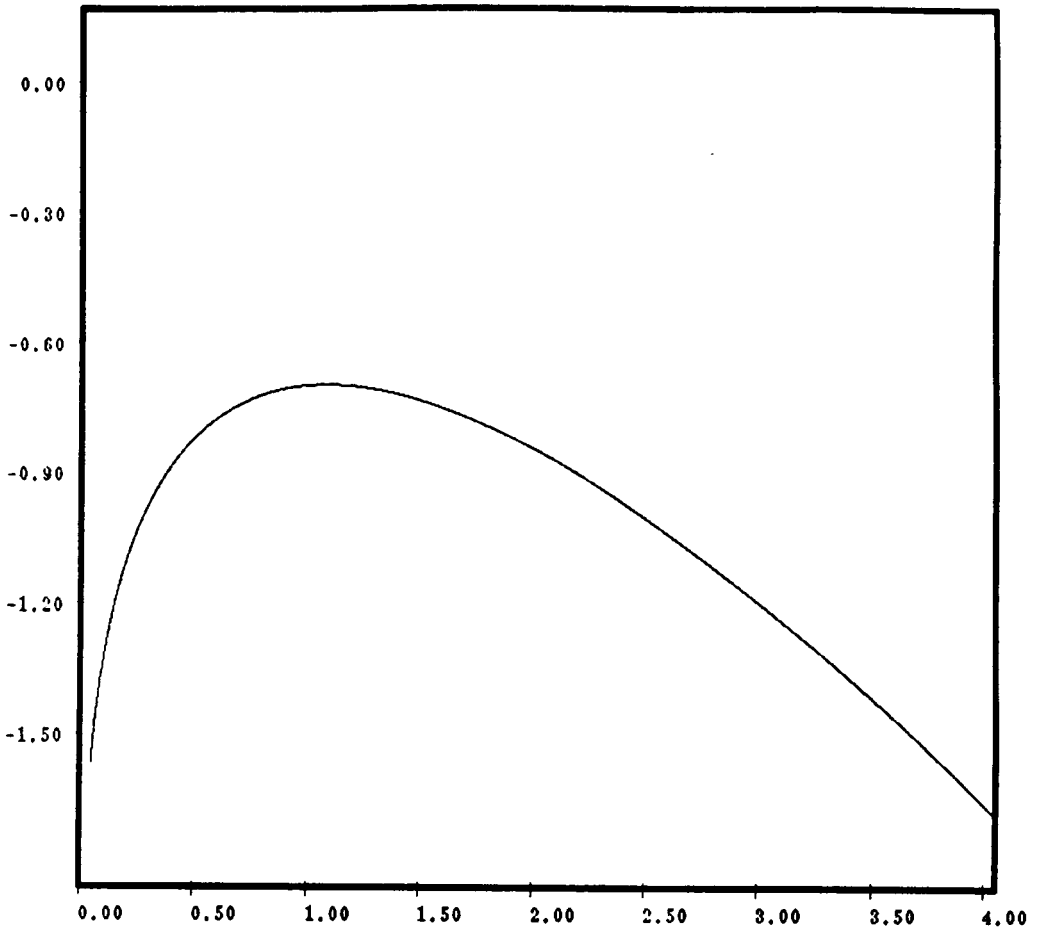

Figure 16. Logarithm of the pulse distribution calculated for the non-Markovian process. The horizontal axis is n/1000.

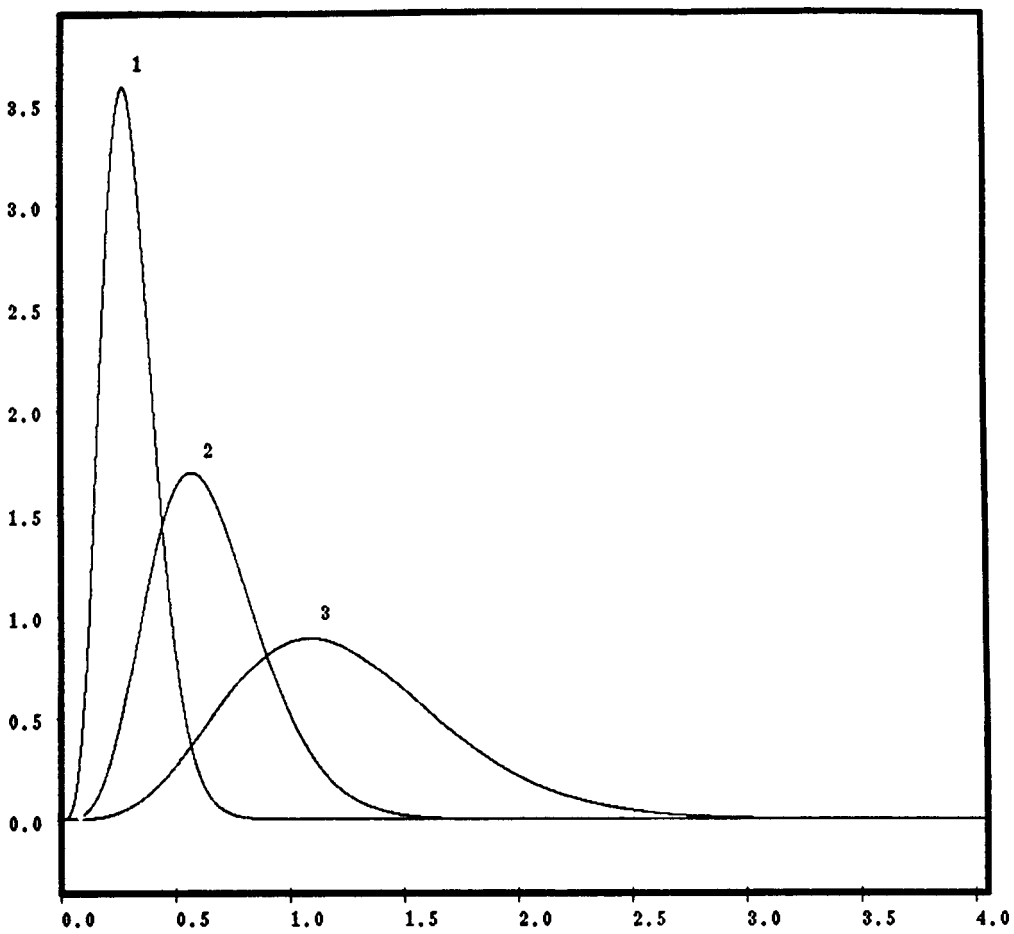

Figure 17. The pulse distribution as a function of position. Curves 1,2, and 3 correspond to t=0.800, t=0.900, and t=0.985, respectively. The horizontal axis is n/1000.

9.4 Discussion

The discussion of the results of the last section is addressed according to two topics. First, the sensitivity of the computed h(n) to the phenomenological parameters is discussed. Second, the interpretation of the computed h(n) with respect to standard distributions is presented.

The parameters r, x_c, and $\langle x_c \rangle$ chosen for this model resulted in a calculated gain lower, by an order of magnitude, than the observed gain. The computed gain would be increased by increasing the branching rate factor r, by decreasing the respective critical distances x_c and $\langle x_c \rangle$, or both. These two conditions would be a step towards more realistically modeling the SSPM, independent of data-matching considerations. First, the distance chosen here for $\langle x_c \rangle$ corresponds to a mean path length of 200 Å, which may be as much as four times larger than the appropriate value for the SSPM. In reduced units, more realistic values for x_c and $\langle x_c \rangle$ should each be found between 0.01 and 0.02. Second, the choice of r = 30 is unrealistically low, for it corresponds to an avalanche spatially confined to a cylinder the length of the avalanche region with a diameter on the order of γ, the neutral cross-section, (since there are, an average, 32 impurity atoms in such a cylinder). Although the spatio-temporal distribution of the carriers in an SSPM pulse is unknown, it surely is not confined to such a narrow cylinder. On the other hand, as mentioned earlier, the phenomenological minimum critical distance x_c decreases with position in an inhomogeneous field. Although this variation is not expected to be dramatic, small variations in x_c may have a large effect on the gain. For the homogeneous field and fixed r, only a 50% decrease in x_c and $\langle x_c \rangle$, respectively, is needed to increase the gain (at t=1) by a factor of 10. Regrettably, such realism cannot immediately be pursued computationally, due to the burden that such a computation would place on the storage capacity of most supercomputers. The function p(n,t;1) is stored in an array of nT words long, where T is the number of intervals used in the numerical integration of Eq. 9.3.2. For T = 512, no pulse of more than 6,000 carriers could be accommodated on a computer restricted to 4 million words in memory. The calculation of h(n) where $\langle n \rangle$ = 15,000 requires at least 25 million words to adequately represent p(n,t). A virtual-memory supercomputer such as the CYBER 205, or a computer attached to a solid-state storage device, could be employed to make such calculations, however.

Such calculations should not be pursued until a more concrete determination of the parameters r, x_c, and $\langle x_c \rangle$ is made. A realistic determination of these parameters could be made via the Boltzmann equation.[8]

Although the Boltzmann equation does not adequately treat non-Markov transport, the non-Markov dynamics of the avalanche are expected to be evident primarily in the collective properties (e.g. p(n,t;1)) rather than in single-carrier properties such as r, x_c, and $\langle x_c \rangle$. In so far as the immediate goal of this work is concerned, further calculations are unnecessary, since it has been shown that a relatively small history-dependence in the branching (i.e., impact-ionization) rate radically alters the Markov result and generates a pulse distribution strikingly similar in shape to that observed in SSPM's. Further, the results portrayed in Figs. 15 and 17 probably scale with increasing r and diminished critical distances, (which in turn increase the gain). The development of h(n) as a function of position shown in Fig. 17 can be (and has been) alternatively be reproduced as a function of increasing r, for appropriate fixed t, x_c and $\langle x_c \rangle$. Such a trend balances the tendency of h(n), for fixed t and r, to assume a more exponential shape with decreasing x_c and $\langle x_c \rangle$, which corresponds to decreasing t in Fig. 17. The combination of these trends suggest that the observed distribution shown in Fig. 11 should be reproduced with appropriately smaller critical distances and larger rates r, a choice which, as noted above, indeed corresponds more closely to the actual device than the choices-of-convenience made for Figs. 15 and 17.

The second topic of concern is the relation between h(n) to standard distributions. It is tempting to begin with standard two-moment distribution, i.e., distributions which require only the first two central moments $\langle n \rangle$ and $\sigma^2 \equiv \langle (n-\langle n \rangle)^2 \rangle$. Fig. 18 shows the computed p(n,t=0.985;1) and the corresponding normal distribution,

$$\eta(\Delta) = (2\pi\sigma^2)^{-1/2} \exp(-\Delta^2/2),$$

where $\Delta = (n-\langle n \rangle)/\sigma$ and $\langle n \rangle$ and σ are taken from Table V. The (least-squares) best fit of the normal distribution does not fare much better, representing a compromise between curves 1 and 2 in Fig. 18. Since both the computed and observed distributions have an appreciable skew (evident in the long tail for large n), non-centro-symmetric distributions were attempted. The best of these was the Weibull distribution $\omega(n)$, i.e.,

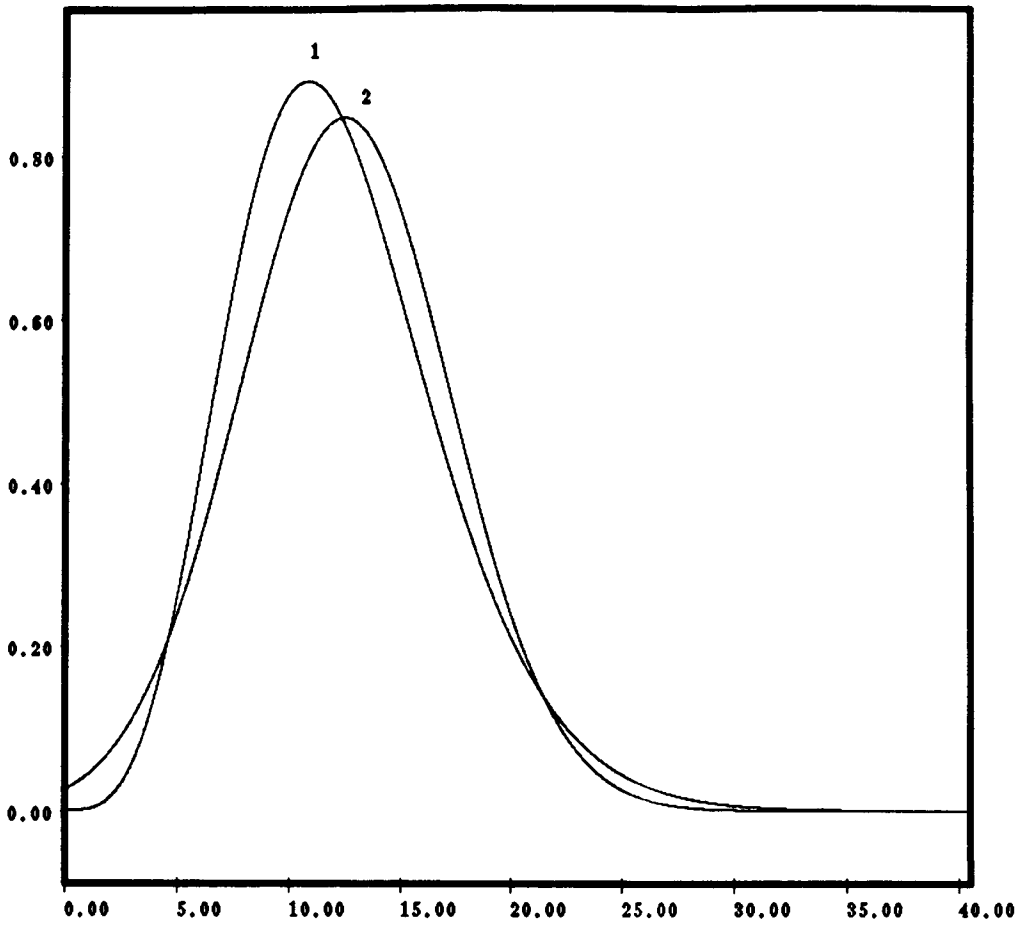

Figure 18. Curve 1 shows the computed h(n). Curve 2 shows the normal distribution with the gain and dispersion (variance) matched to the computed h(n). The horizontal axis is n/100.

$$\omega(n) = ab^{-a}n^{a-1} \exp(-n/b)^a,$$

where $\langle n \rangle = b\Gamma(1+1/a)$, $\sigma^2=b^2(\Gamma(1+2/a)-\Gamma^2(1+1/a))$, and $\Gamma(n+1)=n!$. The corresponding Weibull distribution is compared with the computed h(n) in Fig. 19. Neither the normal nor the Weibull distribution (nor apparently any other two moment distribution) adequately represents either the observed or computed h(n). This is evident also from the large values reported for the skew and the kuritosis, which would each be zero for the normal distribution.[9] The skew κ_1 and kuritosis κ_2, defined respectively by $\kappa_1 \equiv \langle (n-\langle n \rangle)^3 \rangle / \sigma^3$ and $\kappa_2 = \langle (n-\langle n \rangle)^4 \rangle / \sigma^4 - 3$, contain respectively all the third and fourth moment information. If h(n) is regarded as a perturbation to the normal distribution, for example, then the skew and kuritosis might be used to adjust curve 2 in Fig. 18 to match the computed h(n). The Edgeworth series[9] is the most rapidly converging perturbation series of moments for the normal distribution η, namely,

$$E(n) = \eta(\Delta) - \kappa_1/3!\ \eta^{(3)}(\Delta) + \kappa_2/4!\ \eta^{(4)}(\Delta) + 10\kappa_1^2/6!\ \eta^{(6)}(\Delta),$$

where $\eta^{(m)}$ is the m^{th} derivative of η. With the large values of κ_1 and κ_2 found in Table II, however, E(n) actually provides a worse fit than η to the data. Evidently h(n) is not a low-order perturbation of the normal distribution. It is likely that no four-moment distribution will provide an adequate representation of either the observed or computed h(n). Pearson has shown that if a distribution p(υ) satisfies the differential equation

$$p'(\upsilon) = R^{(4)}(\upsilon)\ p(\upsilon),\quad R^{(4)}(\upsilon) = \frac{a_1+\upsilon}{a_2+a_3\upsilon+a_4\upsilon^2}$$

then p may be determined by its four moments.[9] Fig. 20 shows log R, where $R(n) = d\log(h(\upsilon))/d\upsilon|_{\upsilon=n}$ for the computed h(n).

The best fit of $R^{(4)}(n)$ to the computed R(n) fails to adequately describe R(n), and further, fits of $R^{(m)}(n)$ for m up to 10 also failed to adequately represent R. An examination of log R reveals that R must contain a factor which decreases exponentially with n, rather than according to a simple power law. Fig. 20 therefore indicates that no distribution built from a small number (or possibly any finite number) of moments will adequately represent h(n).

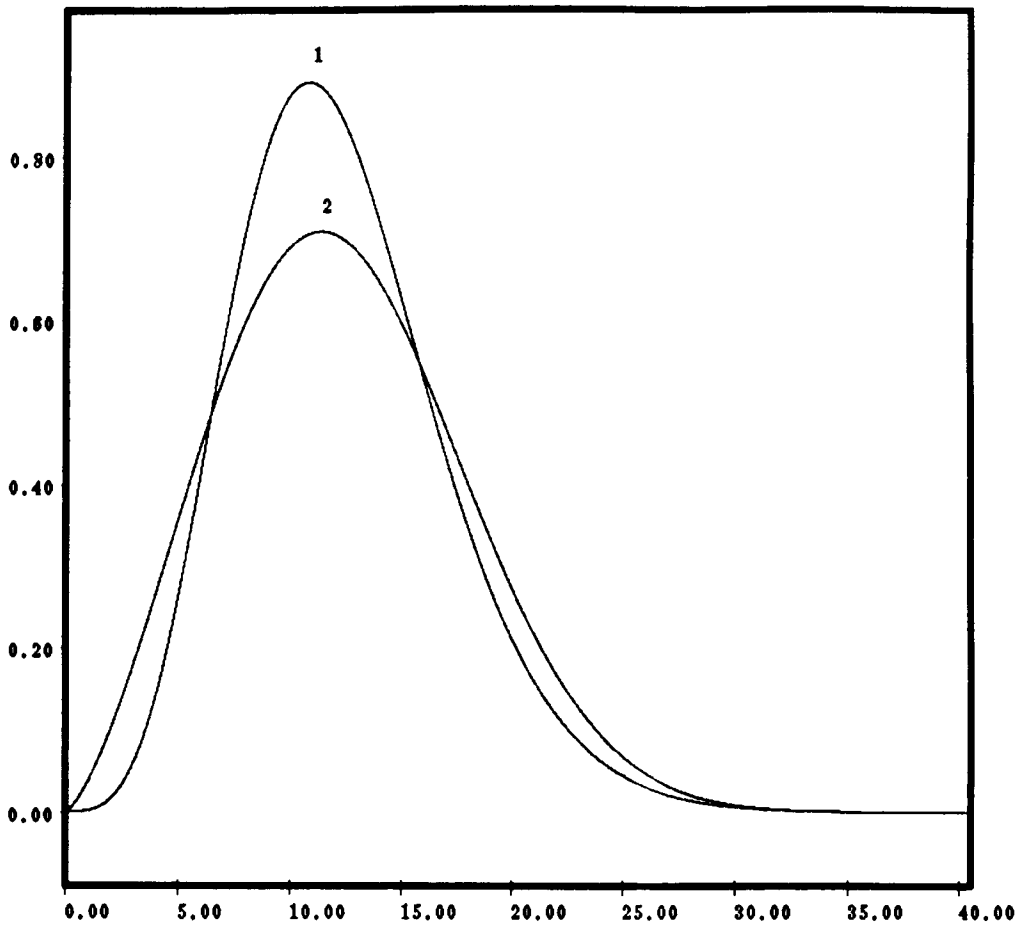

Figure 19. As in Figure 15, curve 2 corresponds to the Weibull distribution which matched the mean and the mode.

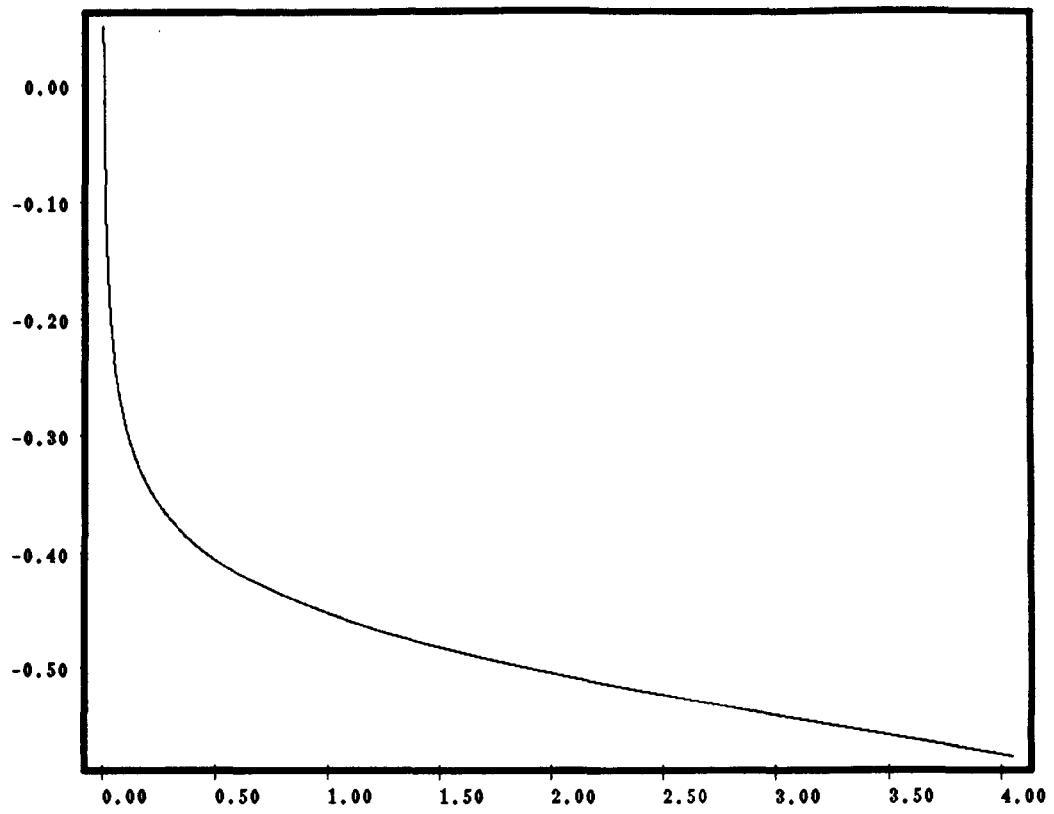

Figure 20. log R, as defined in the text. The horizontal axis is n/1000.

The difficulty with such fits may be examined in another way, with the characteristic function[10]

$$\phi(x) = \sum_{n=0} \exp(2\pi i n x/N)\, h(n+1).$$

Fig. 21 shows the real and imaginary parts of the computed ϕ for $h(n) = p(n,t=0.985;1)$. In general,

$$\phi(x) = \exp\left(\sum_{m=1} \frac{k_m}{m!}(ix)^m\right),$$

where the k_m are the cumulants, which are in turn directly related to the central moments $\langle(n-\langle n\rangle)^m\rangle$. In particular, $k_1=\langle n\rangle$, $k_2=\sigma^2$, $k_3=\langle(n-\langle n\rangle)^3\rangle$, and $k_4=\langle(n-\langle n\rangle)^4\rangle-3\sigma^4$. For the normal distribution η, $k_{m>2}=0$, so the characteristic function is

$$\phi_\eta(x) = \exp(i\langle n\rangle x-\frac{\sigma^2}{2}x^2).$$

However, neither the real nor the imaginary parts of the computed ϕ closely resemble ϕ_η, and with such large values of k_3 and k_4 (which may be found from κ_1 and κ_2 in Table V), an expansion of ϕ_η with only a few cumulants has little hope of adequately representing ϕ, and therefore, of h. Figs. 18 through 21 all vividly demonstrate that h(n) should not be casually described as a normal distribution, or by any of the standard two and four moment distributions commonly discussed in textbooks. This information puts important restrictions on modeling which might otherwise have produced standard distributions. It is satisfying to note that the history-dependent model described in the last section generates an h(n) which captures so many non-standard features of the observed h(n). Nevertheless, it is still desirable to discover a compact representation for the computed h(n). One last attempt to do this employs the generating function of h(n), namely,

$$H(z) = \sum_{n=0} h(n+1)z^n.$$

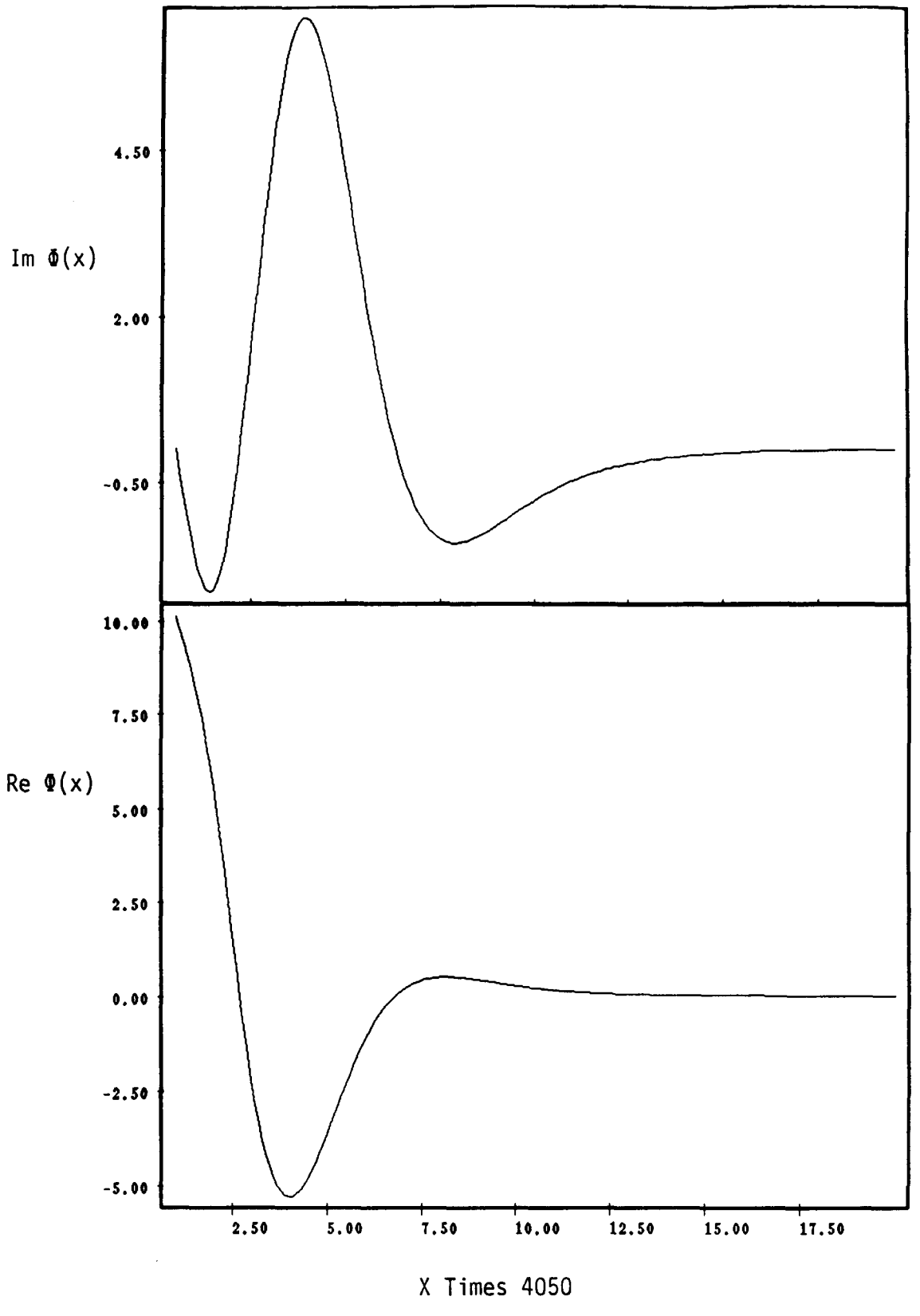

Figure 21. Real and Imaginary Parts of $\Phi(x)$.

For the Markov case, the generating function for $p(n,t;1)$ (t fixed) is[4][5]

$$p(z) = \sum_{n=0} p(n+1,t;1) = \frac{z}{q_t(1-z(1-1/q_t)}, \quad q_t = \int_0^t ds\ \alpha(s).$$

A reasonable hope is that even the non-Markov $H(z)$ can (for $m=1$) be approximated by a convergent sequence (in the degree of the numerator and denominator) rational functions. The existence of a convergent rational function representation, it turns out, cannot be guaranteed for $H(z)$, but is guaranteed[14] for

$$F(z) = \sum_{j=0} f_j z^j, \text{ where } f_j = \sum_{k=0}^{j} 4^{-j}\binom{2j}{j-k} h(k+1).$$

Then, if z_c is the smallest (in absolute value) real pole of $F(z)$,

$$z_c^{-1} = \lim_{n\to\infty} f_n^{1/n},$$

and so[14] $f_n \cong \exp(an+b_1 n^{1/2}+b_2 n^{1/3}+\ldots-c\ \log(n)+k)$, where $a = -\log(z_c)$. With a functional fit to f_j performed in this manner, the $h(k)$ may be found recursively from the f_j. While this is a general procedure, it often suffers from accumulated floating-point errors inherent in machine-based computations, as in the case attempted here.

10.0 CONCLUSIONS

The operating conditions suitable for space-based astronomy applications using the SSPM were determined. In order to maximize the SSPM's dynamic range, the device should be operated at the low end of the usable temperature range. For the devices characterized in this study, the recommended operating temperature is 7 K. To maximize quantum efficiency at this temperature, the highest bias voltage that can be applied without a significant risk of overloading the device is 7.0 V. A monostable multivibrator (one-shot) triggered on the SSPM output pulses can be used to effectively eliminate noise caused by fluctuations in bias current and pulse height.

The avalanche of conduction-band electrons in the SSPM grows by the successive impact-ionization of randomly distributed neutral impurities heavily concentrated in a region about 4 microns long (measured along the direction of the electric field).

The impact-ionization process requires electrons to attain a threshold; this requirement introduces a minimum critical distance from their generation over which the electrons must travel before impact-ionization of neutral impurities can occur. Scattering of sub-threshold carriers together with the random distribution of impurities conspire to produce a distribution of critical impact-ionization distances. A model critical distance distribution has been developed and incorporated into a non-Markov branching process appropriate for non-interacting carriers in a homogeneous electric field in one spatial dimension. The numerical solution of this process demonstrates that a critical distance distribution concentrated over distances as small as a few per cent of the avalanche region's length is sufficient to dramatically alter the distribution of the number of electrons in the pulse from the Markov result. The computed number distribution reproduces the qualitative features of the observed distribution for reasonable parameters, showing a trend towards quantitative agreement for a more realistic if less convenient choice of parameters.

Although the model does not account for carrier-carrier interactions, such interactions are expected to be important for very high gain devices e.g., $\langle n \rangle \geq 50{,}000$. The effect of these interactions is expected to be evident in the truncation of the long large-n tail observed in the number distribution for lower-gain devices. In fact, the number distribution observed for such high gain devices more closely resembles the normal distribution, and the large-n tail appears to be suppressed.

Future work should investigate the effect of an inhomogeneous electric field. Such a field alters the critical distance distribution with position, and corresponds more closely to the environment in the SSPM. Because the variation is expected to be gentle, the qualitative results found for the homogeneous field would be expected to repeat for the inhomogeneous field. More importantly, microscopic ensemble simulations of the three dimensional avalanche via the Boltzmann equations should be pursued. Although the Boltzmann dynamics are essentially Markovian, and the avalanche is essentially a non-Markovian process, the non-Markov dynamics are expected to be evident primarily in collective properties. The single-carrier properties (e.g., critical distances, mobility) are therefore expected to still be well-approximated by the Boltzmann equations. The Boltzmann equation could be used to generate a critical impact-ionization distance distribution based upon only microscopic parameters, and single-carrier dynamics, which could subsequently be employed in the non-Markov process modeled above.

The Boltzmann equation also permits the investigation of carrier-carrier interactions which, in a sufficiently large and concentrated pulse, could induce a collapse of the electric field and thereby limit the growth of the avalanche. Such a calculation would provide a qualitative assessment of the importance of scattering and acceleration delays vs. that of carrier-carrier interactions. Such issues are crucial for the design of improvements to the SSPM.

11.0 REFERENCES

[1] M. D. Petroff, M. G. Stapelbroek and W. A. Kleinhans, U. S. Patent Number 4,586,068, Filed Oct. 7, 1983, Granted Apr. 29, 1986.

[2] M. D. Petroff, M. G. Stapelbroek, and W. A. Kleinhans, Appl. Phys. Lett., (submitted, 1987).

[3] F. Capasso, in "Semiconductors and Semimetals", vol. 22, part D, p. 1 (1985, Academic Press, NY).

[4] T. E. Harris, "The Theory of Branching Processes" (1963, Springer Verlag, Berlin); S. Karlin, "A First Course in Stochastic Processes" (1968, Academic Press, NY).

[5] W. Feller, "An Introduction to Probability Theory and its Applications", Vol. 1, 3d ed. (1968, John Wiley, NY); E. C. Zachmanoglou and D. W. Thoe, "Introduction to Partial Differential Equations", (1976, Wilkins and Wilkins, Baltimore).

[6] D. G. Kendall, J. London Math. Soc. 41 (1966) 385.

[7] G. A. Morton and J. A. Mitchell, RCA Rev. 9 (1948) 632; F. J. Lombard and F. Martin, Rev. Sci. Instr. 32 (1961) 200.

[8] C. Jacoboni and L. Reggiani, Rev. Mod. Phys. 55 (1983) 645.

[9] H. Cramer, "Mathematical Methods of Statistics", (1946, Princeton University).

[10] S. Chandrasekhar, Rev. Mod. Phys. 15 (1943) 86.

[11] W. Shockley, Solid State Electron. 2 (1961) 35.

[12] N. van Kampen, "Stochastic Processes in Physics and Chemistry", (1981, North-Holland, NY).

[13] G. A. Baker, Adv. Theor. Phys. 1 (1965) 1.

[14] A. J. Guttmann and D. S. Gaunt, J. Phys. A. 11 (1978) 949.

12.0 ABSTRACT

SSPM detectors were tested under low-background, low temperature conditions to determine the conditions producing optimal sensitivity in a space-based astronomy system such as a liquid-helium-cooled telescope in orbit. Detector temperatures varied between 6 and 9 K, with background flux ranging from 10^{13} to $<10^{6}$ photons/cm^2-s. Measured parameters included quantum efficiency, noise, dark current and spectral response.

Experimental data were reduced, analyzed and combined with existing data to build an SSPM data base. The results were compared to analytical models of SSPM performance where appropriate models existed.

A phenomenological model of the SSPM avalanche process which predicts the shape of the observed pulse distribution is presented. An accurate prediction of this pulse distribution requires the inclusion of small history-dependent effects on the carrier transport, effects which are neglected in the traditional (Markovian) treatments. The model clarifies the consequences of carrier scattering for the development of the avalanche.

NASA National Aeronautics and Space Administration

Report Documentation Page

1. Report No.	2. Government Accession No.	3. Recipient's Catalog No.
NASA CR- 177465		

4. Title and Subtitle
STUDY OF SOLID STATE PHOTOMULTIPLIER

5. Report Date
August 1987

6. Performing Organization Code

7. Author(s)
K. M. Hays, R. A. LaViolette

8. Performing Organization Report No.
SC5464.FR

10. Work Unit No.
506-45-31

9. Performing Organization Name and Address
Rockwell International Science Center
P. O. Box 3105
Anaheim, CA 92803-3105

11. Contract or Grant No.
NAS2-12400

13. Type of Report and Period Covered
Final Contractor Report
Jun 1, 1986 - Apr 30, 1987

12. Sponsoring Agency Name and Address
National Aeronautics and Space Administration (RC)
Washington, DC 20546-0001

14. Sponsoring Agency Code

15. Supplementary Notes
Point of Contact: Technical Monitor, John H. Goebel, MS 244-10
Ames Research Center, Moffett Field, CA 94035
(415) 694-6525 or FTS 464-6525

16. Abstract

Arsenic-doped silicon (Si:As) solid-state photomultiplier (SSPM) detectors were tested under low-background, low-temperature conditions to determine optimal sensitivity in a space-based astronomical system such as a liquid-helium-cooled telescope. Detector temperatures varied between 6 and 9 K, with background flux ranging from 10^{13} to $<10^{6}$ photons/cm^2-s. Measured parameters included quantum efficiency, noise, dark current, and spectral response. These data were reduced, analyzed and combined with previous data to build an SSPM data base. The results were compared to analytical models of SSPM performance where appropriate models existed.

A phenomenological model of the SSPM avalanche process which predicts the shape of the observed pulse distribution is presented. An accurate prediction of this pulse distribution requires the inclusion of small history-dependent effects on the carrier transport, effects which are neglected in the traditional (Markovian) treatments. The model clarifies the consequences of carrier scattering for the development of the avalanche.

17. Key Words (Suggested by Author(s))	18. Distribution Statement
Infrared detector, Extrinsic silicon, Photomultiplier detector, Infrared astronomy	Unclassified - Unlimited STAR category 35

19. Security Classif. (of this report)	20. Security Classif. (of this page)	21. No. of pages	22. Price
Unclassified	Unclassified	53	